

# Cross-Seasonal Impact of SST Anomalies over the Tropical Central Pacific Ocean on the Antarctic Stratosphere

Yucheng Zi<sup>1,2,3,4</sup>, Zhenxia Long<sup>3</sup>, Jinyu Sheng<sup>2</sup>, Gaopeng Lu<sup>4</sup>, Will Perrie<sup>2,3,5</sup>, and Ziniu Xiao<sup>1,4</sup>

*Correspondence:* Zhenxia Long (Zhenxia.Long@dfo-mpo.gc.ca) and Ziniu Xiao (xiaozn@lasg.iap.ac.cn)

<sup>1</sup> State Key Laboratory of Earth System Numerical Modeling and Application, Institute of Atmospheric Physics, Chinese Academy of Sciences, Beijing, China

<sup>2</sup> Department of Oceanography, Dalhousie University, Halifax, Nova Scotia, Canada

<sup>3</sup> Fisheries and Oceans Canada, Bedford Institute of Oceanography, Dartmouth, Nova Scotia, Canada

<sup>4</sup> School of Earth and Space Sciences, University of Science and Technology of China, Hefei, China

<sup>5</sup> Department of Engineering Mathematics & Internetworking, Dalhousie University, Halifax, Canada

~~<sup>4</sup> School of Earth and Space Sciences, University of Science and Technology of China, Hefei, China~~

~~<sup>2</sup> Department of Oceanography, Dalhousie University, Halifax, Nova Scotia, Canada~~

~~<sup>3</sup> Fisheries and Oceans Canada, Bedford Institute of Oceanography, Dartmouth, Nova Scotia, Canada~~

~~<sup>4</sup> State Key Laboratory of Earth System Numerical Modeling and Application, Institute of Atmospheric Physics, Chinese Academy of Sciences, Beijing, China~~

~~<sup>5</sup> Department of Engineering Mathematics & Internetworking, Dalhousie University, Halifax, Canada~~

21 November 2025

26

27 **Abstract**

28 In this study we examine the cross-seasonal effects of boreal winter sea surface temperature  
 29 (SST) anomalies over the central tropical Pacific (Niño 4 region) on Antarctic stratospheric  
 30 circulation and ozone transport during the subsequent austral winter using ERA5 reanalysis of 45  
 31 years (1980–2024). Our analyses show that warm (cold) SST anomalies in Niño 4 region during  
 32 December–February are associated with ~~mid- and high-latitude polar~~ stratospheric warming  
 33 (cooling), a ~~contracted/weakened~~ (~~strengthened/expanded~~) stratospheric polar vortex (SPV), and  
 34 enhanced (suppressed) polar ozone concentrations during July–September of the subsequent year.  
 35 This delayed response is mediated by a Pacific–South America (PSA) teleconnection, which  
 36 excites planetary waves that propagate upward into stratosphere and modify the Brewer–Dobson  
 37 circulation. In addition, as the influence of ~~Niño~~Niño 4 SSTs on the PSA teleconnection pattern  
 38 diminishes during July–September, surface heat feedback at mid and high latitudes becomes  
 39 critically important for planetary waves. Specifically, persistent South Pacific SST warming and  
 40 sea-ice loss over the Amundsen and Ross Seas reinforce planetary waves by releasing heat from  
 41 ocean into atmosphere. A multivariate regression statistical model using ~~predif~~actors of boreal  
 42 winter ~~Niño~~Niño 4 SST, and June PSA, ~~June South Pacific SST, and May–June sea-ice~~  
 43 ~~concentration (SIC)~~ indices explain approximately 35 % of the variance in austral winter  
 44 stratospheric temperatures. These findings highlight a previously underexplored pathway through  
 45 which tropical Pacific SST anomalies modulate Antarctic stratospheric dynamics ~~and chemistry~~  
 46 on seasonal timescales. ~~This implies a new insight into tropical polar coupling and provides a~~  
 47 ~~potential signal for extended range forecasts of ozone depletion risk.~~

48

49 **Keywords:** El Niño–Southern Oscillation (ENSO); Stratospheric warming; Stratospheric polar  
 50 vortex (SPV); ~~Antarctic ozone~~; Pacific–South America (PSA) pattern; Multivariate regression

51

## 52 **1 Introduction**

53 The Antarctic stratospheric circulation is largely governed by the wintertime Stratospheric  
54 Polar Vortex (SPV), which is a major driver of weather and climate variability across the Southern  
55 Hemisphere (Baldwin et al., 2021). Compared to its Northern Hemisphere counterpart, the  
56 Antarctic SPV is generally more stable, owing to weaker thermal contrasts between the ocean and  
57 land. Despite this stability, the Antarctic SPV exhibits considerable interannual variability  
58 (Domeisen et al., 2019; Baldwin et al., 2021). Furthermore, the Antarctic stratosphere plays a  
59 crucial role in modulating weather and climate in the Southern Hemisphere through the seasonal  
60 evolution of SPV and its dynamics processes and interaction with ozone chemistry (Thompson et  
61 al., 2005; Solomon et al., 2016).

62 Previous studies revealed large interannual variations and long-term trends in the SPV,  
63 stratospheric temperatures, and ozone concentrations (Karpetchko et al., 2005). ~~In the late 20th~~  
64 ~~century, anthropogenic emissions of chlorofluorocarbons (CFCs) cooled the polar stratosphere,~~  
65 ~~intensified the SPV, and caused severe springtime ozone depletion, which resulted in the formation~~  
66 ~~of the Antarctic ozone hole (Solomon et al., 2016). After the implementation of the Montreal~~  
67 ~~Protocol for phasing out production and consumption of ozone-depleting substances, signs of ozone~~  
68 ~~recovery have emerged, accompanied by a gradual weakening of the SPV and associated~~  
69 ~~stratospheric warming (Solomon et al., 2016).~~ Superimposed on the long-term trends of SPV are  
70 substantial interannual variations and extreme events. For instance, exceptionally weak SPV  
71 episodes triggered by sudden stratospheric warmings (SSWs) occurred respectively in 2002, 2010,  
72 2019, and 2024 (Thompson and Solomon, 2002; Esler et al., 2006; Laat and Weele 2011; Shen et  
73 al., 2020; Zi et al., 2025), and an unusually strong SPV event driven by the pronounced ozone  
74 depletion occurred in 2020 (Lim et al., 2024).

75 Several natural factors contribute to the above-mentioned SPV variability. The phase of the  
76 Quasi-Biennial Oscillation (QBO), for instance, modulates planetary-wave propagation and can  
77 either strengthen or weaken the SPV (Kuroda et al., 2007). El Niño–Southern Oscillation (ENSO)  
78 events also leave distinct warm- and cold-year signatures on Antarctic stratospheric temperatures  
79 ~~and ozone~~ through changes in tropospheric wave forcing and the Brewer–Dobson (B-D) circulation  
80 (Yang et al., 2015; Stone et al., 2022; Rao et al., 2023; Wang et al., 2025). Previous studies also  
81 suggest sea ice can have significant impact on the SPV (e.g., Rea et al., 2024; Song et al., 2025;

82 [Sun et al., 2015](#)), with implications for Southern Hemisphere climate variability. In addition, solar-  
83 cycle variability contributes to interannual modulation by altering ultraviolet irradiance and  
84 stratospheric heating rates (Kuroda et al., 2007). Alongside these natural drivers, fluctuations in the  
85 atmospheric burdens of ozone-depleting substances and greenhouse gases continue to influence  
86 both the magnitude and nature of Antarctic stratospheric variability (Singh and Bhargawa, 2019).

87 ENSO is the most prominent mode of interannual climate variability (Wang, 2018).  
88 Developing in boreal autumn and peaking in winter, ENSO influences the global weather patterns  
89 through atmospheric teleconnections (McPhaden et al., 2006). It also modulates the SPV primarily  
90 via the Pacific–North America (PNA) and Pacific–South America (PSA) wave trains (Garfinkel  
91 and Hartmann, 2008; Ineson and Scaife, 2009; Barriopedro and Calvo, 2014; Polvani et al., 2017;  
92 Song and Son, 2018; Zhang et al., 2022). In the Northern Hemisphere, El Niño events enhance  
93 tropical convection and amplify the PNA pattern, strengthening the Aleutian Low, which in turn  
94 increases upward wave activity and weakens the SPV (Garfinkel and Hartmann, 2008; Butler and  
95 Polvani, 2011; Zhang et al., 2022). In the Southern Hemisphere, central Pacific (CP–type) El Niño  
96 events during September–February enhance convection near the South Pacific Convergence Zone  
97 (SPCZ), which triggers the PSA wave trains that can weaken the Antarctic SPV, resulting in  
98 stratospheric warming and ozone enhancement (Hurwitz et al., 2011a,b; Yang et al., 2015; Manatsa  
99 and Mukwada, 2017; Domeisen et al., 2019; Ma et al., 2022). In contrast, Eastern Pacific (EP–type)  
100 El Niño events were found to produce weaker stratospheric responses (Hurwitz et al., 2011a;  
101 Zubiaurre and Calvo, 2012).

102 Although many studies were made on the Antarctic stratosphere’s simultaneous or 1-2 months  
103 lag responses to ENSO from September to February (L’Heureux and Thompson, 2006; Silvestri  
104 and Vera, 2009; Hu and Fu, 2010; Fogt et al., 2011; Lin et al., 2012; Kim et al., 2017; Ma et al.,  
105 2022), our knowledge remains very limited on the ENSO’s cross–seasonal and delayed effects  
106 (Manatsa and Mukwada, 2017; Niu et al., 2023). Some previous studies found that delayed ozone  
107 responses occur in the year following an ENSO event (Lin and Qian, 2019), while others suggested  
108 that tropical sea surface temperature (SST) anomalies as early as June can influence stratospheric  
109 circulation later in the year (Grassi et al., 2008; Evtushevsky et al., 2015; Lim et al., 2018; Stone  
110 et al., 2022). Yang et al. (2015) examined correlations between ENSO and Antarctic stratospheric  
111 temperatures during July–September, but these were primarily interpreted as concurrent responses.

112 Despite these studies, the physical mechanisms by which ENSO events in boreal winter influence  
 113 the Antarctic stratosphere during the following austral winter (July–September) remain poorly  
 114 understood. Better understanding of ENSO’s delayed impact is particularly important, since the  
 115 SPV in the austral winter is strongest and most susceptible to dynamical disturbances, with  
 116 significant implications for ~~forecast of Antarctic stratospheric extreme events~~~~polar ozone chemistry~~  
 117 (Lin et al., 2009; Thompson et al., 2011).

118 The main objective of this study is to examine how the boreal winter SST anomalies (SSTs)  
 119 influence the Antarctic stratosphere during the following austral winter, with a special emphasis on  
 120 mechanisms by which ~~NiñoNiño~~ 4 SSTs modulate polar stratospheric dynamics ~~and ozone~~  
 121 ~~transport~~, and associated planetary wave propagation and mid-latitude sea-air interactions. ~~A multi-~~  
 122 ~~regression analysis will also be used to evaluate the potential for predicting stratospheric~~  
 123 ~~temperature anomalies based on early season climate indicators.~~The structure of this paper is as  
 124 follows. Section 2 describes the data and methodology. Section 3 presents quantification of the  
 125 ENSO–Antarctic stratosphere relationship. Section 4 shows an examination of the underlying  
 126 dynamical mechanisms. Section 5 presents the multivariate regression analysis. Section 6 is a  
 127 summary and conclusion.

128

## 129 **2. Data and methods**

### 130 **2.1 Data**

131 The 6-hourly and monthly-mean atmospheric variables in the 45-year period 1980–2024  
 132 extracted from the ERA5 reanalysis (Hersbach et al., 2023a,b) are used in this study. This reanalysis  
 133 with a horizontal resolution of  $1^\circ \times 1^\circ$  was generated by the European Centre for Medium-Range  
 134 Weather Forecasts (ECMWF). These atmospheric variables at 37 vertical pressure levels include  
 135 the geopotential height, horizontal and vertical winds, temperature, sea level pressure (SLP), ozone  
 136 mass mixing ratio, total column ozone (TCO<sub>3</sub>), net surface downward short-wave radiation flux,  
 137 net surface upward long-wave radiation flux, latent and sensible heat fluxes, outgoing long-wave  
 138 radiation flux (OLR). The monthly sea surface temperature (SST) and sea-ice concentration (SIC)  
 139 during the same study period were also extracted from ERA5 reanalysis.

140 Several indices (such as ~~NiñoNiño~~ 3, ~~NiñoNiño~~ 3.4, and ~~NiñoNiño~~ 4) based on SST anomalies  
 141 averaged over a given region have been used to monitor the dynamic activities in the tropic Pacific

142 (Bamston et al. 1997; Trenberth, 1997). ~~NiñoNiño~~ 3 is the SST anomalies averaged over the region  
 143 between 5 °N ~~and~~ 5 °S and ~~between~~ 150 °W ~~and~~ 90 °W, and has been used for monitoring and  
 144 predicting El Niño ~~and~~ La Niña events (Trenberth, 1997). ~~NiñoNiño~~ 3.4 is the SST anomalies  
 145 averaged over the region between 5 °N–5 °S and 170 °W–120 °W, and has been used as the primary  
 146 index for monitoring ENSO due to its ability to capture basin-scale variability (Bamston et al. 1997).  
 147 ~~NiñoNiño~~ 4 is the SST anomalies averaged over the region between 5 °N–5 °S and 160 °W ~~E~~–  
 148 150 °W, which is to monitor SST anomalies in the central equatorial Pacific. In this study, the  
 149 SST indices for ~~NiñoNiño~~ 3, ~~NiñoNiño~~ 3.4, and ~~Niño~~ 4 were obtained from the HadISST1.1 dataset  
 150 (Rayner et al., 2003). Since results obtained after filtering the interannual component are similar, no  
 151 filtering has been applied.

152 The Pacific–South America pattern (PSA) index was used to examine stratosphere and  
 153 troposphere interactions, which was derived by projecting area–weighted SLP anomalies south of  
 154 20 °S onto the second Empirical Orthogonal Function (EOF) mode (Mo and Higgins, 1998). All  
 155 anomalies are calculated relative to the 1991–2020 daily and monthly climatology, and all data  
 156 have been detrended. Statistical significance is assessed using the Student's s t-test.

157

## 158 2.2 Method

### 159 2.2.1 E–P flux

160 The Eliassen–Palm (E–P) theorem is used to diagnose interactions between eddies and the  
 161 zonal–mean flow in both the stratosphere and troposphere (Andrews et al., 1987). The E–P flux ( $\vec{F}$ )  
 162 and its divergence ( $\nabla \cdot \vec{F}$ ) are defined:

$$163 \quad \vec{F} = (\vec{F}_\varphi, \vec{F}_p) = r_0 \cos \varphi \left\{ -[u'v'], \frac{f}{[\theta_p]} [v'\theta'] \right\} \quad (1)$$

$$164 \quad \nabla \cdot \vec{F} = \frac{1}{r_0 \cos \varphi} \frac{\partial}{\partial \varphi} (\vec{F}_\varphi \cos \varphi) + \frac{\partial}{\partial p} (\vec{F}_p) \quad (2)$$

165 where  $u$  and  $v$  are the zonal and meridional wind components, respectively, and  $\theta$  is the  
 166 potential temperature.  $\varphi$  and  $p$  denote latitude and pressure, respectively.  $f$  is the Coriolis  
 167 parameter, and  $r_0$  is Earth's radius. Square brackets [ ] indicate zonal averages, and primes (')  
 168 denote deviations from the zonal mean.

169

### 170 2.2.2 Takaya–Nakamura (TN01) wave activity flux

171 The Takaya–Nakamura (2001) wave activity flux (TN01 flux) has been used for determining  
 172 the horizontal propagation of quasi-stationary Rossby waves in a zonally varying background flow  
 173 (Takaya and Nakamura, 2001). The zonal ( $F_x$ ) and meridional ( $F_y$ ) components of TN01 are  
 174 defined as:

$$175 \quad F_x = \frac{p}{2|U^*|r_0^2} \left( \frac{U}{\cos \varphi} \left( \left( \frac{\partial \psi'}{\partial \lambda} \right)^2 - \psi' \frac{\partial^2 \psi'}{\partial \lambda^2} \right) + V \left( \frac{\partial \psi'}{\partial \lambda} \frac{\partial \psi'}{\partial \varphi} - \psi' \frac{\partial^2 \psi'}{\partial \lambda \partial \varphi} \right) \right) \quad (3)$$

$$176 \quad F_y = \frac{p}{2|U^*|r_0^2} \left( U \left( \frac{\partial \psi'}{\partial \lambda} \frac{\partial \psi'}{\partial \varphi} - \psi' \frac{\partial^2 \psi'}{\partial \lambda \partial \varphi} \right) + V \cos \varphi \left( \left( \frac{\partial \psi'}{\partial \varphi} \right)^2 - \psi' \frac{\partial^2 \psi'}{\partial \varphi^2} \right) \right) \quad (4)$$

177 where  $\psi$  represents the stream function,  $\lambda$  and  $\varphi$  denote longitude and latitude, respectively, and  
 178  $|U^*|$  is the magnitude of the total horizontal wind velocity.  $U$  and  $V$  are the climatological  
 179 mean zonal and meridional wind components, respectively, while  $p$  is pressure, and  $r_0$  is Earth's  
 180 radius.

181

### 182 2.2.3 Residual mean meridional circulation

183 The Transformed Eulerian–Mean (TEM) formulation suggested by Andrews and McIntyre  
 184 (1976, 1978) has widely been employed for diagnosing the large–scale circulation in the middle  
 185 atmosphere. Different from the conventional Eulerian mean, the TEM framework accounts for eddy  
 186 heat and momentum fluxes, thereby providing a more accurate representation of actual mass  
 187 transport. In particular, the residual mean meridional circulation encapsulates the net effect of both  
 188 mean flow and wave–induced eddy motions, making it especially useful for diagnosing  
 189 stratospheric processes, such as B–D circulation and wave–driven anomalies associated with  
 190 stratospheric warming. It is defined as:

$$191 \quad [v]^* = [v] - \frac{1}{\rho_0} \frac{\partial}{\partial z} \left( \frac{\rho_0 [v'\theta']}{[\theta_z]} \right) \quad (5)$$

$$192 \quad [w]^* = [w] - \frac{1}{r_0 \cos \varphi} \frac{\partial}{\partial \varphi} \left( \frac{\cos \varphi [v'\theta']}{[\theta_z]} \right) \quad (6)$$

193 where  $[v]^*$  and  $[w]^*$  denote the meridional and vertical components of the residual velocity,  
 194 respectively. The vertical coordinate  $z$  is the log–pressure height defined as  $z =$

195  $-H \log \frac{p}{1000 \text{ hPa}}$ , where  $H$  is the scale height ( $\approx 7$  km). All other variables are consistent with  
 196 those defined in Equations (1)–(4).

197

### 198 2.2.4 Residual mean meridional circulation

199 The quasi-geostrophic wave refraction index ( $n^2$ ) is also employed to diagnose the  
 200 propagation characteristics of planetary waves (O'Neill, and Youngblut, 1982). In general,  
 201 planetary waves tend to propagate toward regions with a larger value of the refraction index. The  
 202 formula is given as follows:

$$203 \quad n^2 = \left[ \frac{\bar{q}_\varphi}{r_0(\bar{u} - c)} - \left( \frac{k}{r_0 \cos \varphi} \right)^2 - \left( \frac{f}{2NH} \right)^2 \right] r_0^2 \quad (7)$$

204 where the meridional gradient of the zonal mean potential vorticity  $\bar{q}_\varphi$  is (Albers and Birner,  
 205 2014):

$$206 \quad \bar{q}_\varphi = 2\Omega \cos \varphi - \left[ \frac{(\bar{u} \cos \varphi)_\varphi}{r_0 \cos \varphi} \right]_\varphi + \frac{r_0 \alpha f^2}{R_d} \left( \frac{p\theta \bar{u}_p}{T \theta_p} \right)_p \quad (8)$$

207 Where  $\bar{u}$  is the zonal-mean zonal wind;  $N, H, k, f, \varphi, r_0$  and  $\Omega$  are the buoyancy  
 208 frequency, scale height, zonal wave number, the Coriolis parameter, latitude, Earth's radius and  
 209 angular frequency of Earth, respectively. The subscripts refer to derivatives with respect to the  
 210 given variable and the prime denotes the departure from the zonal mean.

211

### 212 2.2.5 CMIP6 datasets

213 To validate the observational results with model simulations, output from Phase 6 of the  
 214 Coupled Model Intercomparison Project (CMIP6) are examined. Historical simulations were  
 215 performed using fully coupled atmosphere–ocean models forced with observed external drivers,  
 216 including greenhouse gases, aerosols, volcanic eruptions, and solar variability. The analysis focuses  
 217 on monthly mean SST, SIC, and temperature at 10 hPa over the period 1951–2014. A total of 20  
 218 fully coupled CMIP6 models are included: CESM2, CESM2-FV2, CESM2-WACCM, CESM2-  
 219 WACCM-FV2, EC-Earth3-AerChem, EC-Earth3-Veg, EC-Earth3-CC, GISS-E2-1-G, MPI-ESM-  
 220 1-2-HAM, MPI-ESM1-2-LR, E3SM-1-0, E3SM-1-1-ECA, ACCESS-CM2, HadGEM3-GC31-LL,  
 221 BCC-CSM2-MR, CanESM5-1, CAS-ESM2-0, CIESM, FIO-ESM-2-0, SAM0-UNICON. Because

222 these selected CMIP6 models differ in their horizontal resolutions, to ensure consistency across  
 223 datasets, all fields are interpolated onto a uniform 1°×1° latitude–longitude grid to ensure  
 224 consistency across datasets.

225

### 226 3 Impacts of ENSO on stratospheric atmospheric circulation

227 To quantify the cross–seasonal response of the Antarctic stratospheric circulation to ENSO,  
 228 we first correlate three ENSO indices: NiñoNiño 4, NiñoNiño 3.4, and NiñoNiño 3, with the  
 229 stratospheric temperature ( $T_{10-30}$ ) and zonal wind ( $U_{10-30}$ ) over Antarctica during the subsequent  
 230 July–September period. Here,  $T_{10-30}$  refers to the zonal-mean temperature averaged over 60 °S–  
 231 90 °S at 10–30 hPa, and  $U_{10-30}$  refers to the zonal-mean zonal wind averaged over 40 °S–50 °S at  
 232 the same pressure levels (Table 1).

233

234 **Table 1.** Correlation coefficients between NiñoNiño 4, NiñoNiño 3.4 and NiñoNiño 3 indices and zonal-mean  
 235 temperature index ( $T_{10-30}$ ) averaged over 60 °S to 90 °S as well as zonal wind index ( $U_{10-30}$ ) averaged over 40 °S  
 236 to 50 °S at 10–30 hPa.

	$T_{10-30\_Jul}$	$T_{10-30\_Aug}$	$T_{10-30\_Sep}$	$U_{10-30\_Jul}$	$U_{10-30\_Aug}$	$U_{10-30\_Sep}$
<u>NiñoNiño</u> 4_Sep	0.37***	0.36**	0.32**	-0.26*	-0.31**	-0.30**
<u>NiñoNiño</u> 4_Oct	0.35**	0.36**	0.34**	-0.22	-0.29*	-0.32**
<u>NiñoNiño</u> 4_Nov	0.37***	0.40***	0.32**	-0.22	-0.32**	-0.31**
<u>NiñoNiño</u> 4_Dec	0.38***	0.42***	0.35**	-0.24	-0.37***	-0.34**
<u>NiñoNiño</u> 4_Jan	0.42***	0.43***	0.30**	-0.31**	-0.40***	-0.33**
<u>NiñoNiño</u> 4_Feb	0.41***	0.41***	0.31**	-0.30**	-0.38***	-0.32**
<u>NiñoNiño</u> 4_Mar	0.38***	0.39***	0.30**	-0.23	-0.34**	-0.28*
<u>NiñoNiño</u> 3.4_Sep	0.34**	0.26*	0.20	-0.20	-0.21	-0.20
<u>NiñoNiño</u> 3.4_Oct	0.32**	0.27*	0.24	-0.19	-0.21	-0.23
<u>NiñoNiño</u> 3.4_Nov	0.34**	0.29*	0.23	-0.20	-0.23	-0.23
<u>NiñoNiño</u> 3.4_Dec	0.37***	0.31**	0.25*	-0.19	-0.24	-0.23
<u>NiñoNiño</u> 3.4_Jan	0.38***	0.32**	0.21	-0.24	-0.26*	-0.21
<u>NiñoNiño</u> 3.4_Feb	0.38***	0.32**	0.21	-0.25*	-0.26*	-0.21
<u>NiñoNiño</u> 3.4_Mar	0.36**	0.35**	0.25*	-0.23	-0.28*	-0.23
<u>NiñoNiño</u> 3_Sep	0.33**	0.22	0.14	-0.18	-0.17	-0.16
<u>NiñoNiño</u> 3_Oct	0.31**	0.21	0.18	-0.17	-0.16	-0.18
<u>NiñoNiño</u> 3_Nov	0.32**	0.23	0.19	-0.17	-0.18	-0.18
<u>NiñoNiño</u> 3_Dec	0.35**	0.25*	0.21	-0.16	-0.18	-0.18
<u>NiñoNiño</u> 3_Jan	0.35**	0.25*	0.16	-0.20	-0.19	-0.16
<u>NiñoNiño</u> 3_Feb	0.36**	0.27*	0.16	-0.20	-0.19	-0.15

<u>NiñoNiño</u> 3_Mar	0.29*	0.31**	0.20	-0.21	-0.23	-0.19
-----------------------	-------	--------	------	-------	-------	-------

237

238 Note: Colors and asterisks denote statistical significance: red with \*\*\* for the 99 % confidence level,  
 239 bluegreen with \*\* for 95 %, and magenta with \* for 90 %.

240

241 Among the three indices, the NiñoNiño 4 index has the largest correlation with Antarctic  
 242 stratospheric circulations (Table 1). In particular, the NiñoNiño 4 index exhibits a significantly  
 243 positive correlation with the subsequent July–September mean  $T_{10-30}$  index, with correlations from  
 244 September to March reaching the 95 % confidence level. Here, the largest correlation occurs during  
 245 boreal winter (December–February), with correlation coefficients exceeding 0.30 at the 95 %  
 246 confidence level ( $R > 0.30$ ,  $p < 0.05$ ). The January NiñoNiño 4 index shows the highest correlation  
 247 with August  $T_{10-30}$  ( $R > 0.43$ ,  $p < 0.01$ ). Additionally, the December–February NiñoNiño 4 index is  
 248 significantly negatively correlated with the July–September  $U_{10-30}$  index, with the largest negative  
 249 correlation found between the January NiñoNiño 4 and August  $U_{10-30}$  ( $R = -0.40$ ,  $p < 0.01$ ). These  
 250 correlations are consistent with stratospheric warming (cooling) and a weakened (strong)  
 251 Stratospheric polar vortex (SPV) associated with warm (cold) central Pacific SSTs.

252 In comparison with NiñoNiño 4, the NiñoNiño 3.4 index has weaker correlations with  
 253 stratospheric temperature and zonal wind. The January NiñoNiño 3.4 has the highest correlation  
 254 with July  $T_{10-30}$  ( $R \approx 0.38$ ,  $p < 0.01$ ), while the correlation with September  $T_{10-30}$  is not statistically  
 255 significant. Similarly, its correlation with  $U_{10-30}$  is weak, with only a marginally significant negative  
 256 correlation between the January–March NiñoNiño 3.4 index and July–August  $U_{10-30}$  at the 90 %  
 257 confidence level. However, the NiñoNiño 3 index exhibits the weakest correlation with the polar  
 258 stratosphere. While a moderate correlation with  $T_{10-30}$  is observed during July–August, correlations  
 259 in September are very weak and do not exceed the 90 % significance threshold.

260 We next examine the connection of ENSO phases in the preceding boreal winter with the  
 261 Antarctic stratospheric circulation anomalies in July–September for 45 years 1980–2024 (Table 2).  
 262 Here, we define a warm (cold) stratospheric year as the year when the July–September mean  $T_{10-}$   
 263  $30$  index is  $\geq 0.5$  ( $\leq -0.5$ ) standard deviations or when the  $U_{10-30}$  index is  $\leq -0.5$  ( $\geq 0.5$ ) standard  
 264 deviations. During the study period of 45 years, 14 are boreal winter El Niño years, of which 8 are  
 265 followed by stratospheric warming events and 4 by cooling events, corresponding to an occurrence  
 266 rate of 57 % and 28.5 %, respectively. Notably, 6 out of these 8 warming cases occur after central

267 Pacific El Niño events. The remaining two cases, 2015/16 and 2023/24, are classified as eastern  
 268 Pacific El Niño events, but are also accompanied by warm SSTs in the tropical central Pacific. By  
 269 comparison, among 17 boreal winter La Niña years, 11 are followed by stratospheric cooling events  
 270 and 4 by warming events, corresponding to occurrence rates of 65 % and 23.5 %, respectively. Of  
 271 the 13 ENSO-neutral years, four are associated with stratospheric warming events and another four  
 272 with cooling events, indicating no clear preference for either condition during neutral years.

273

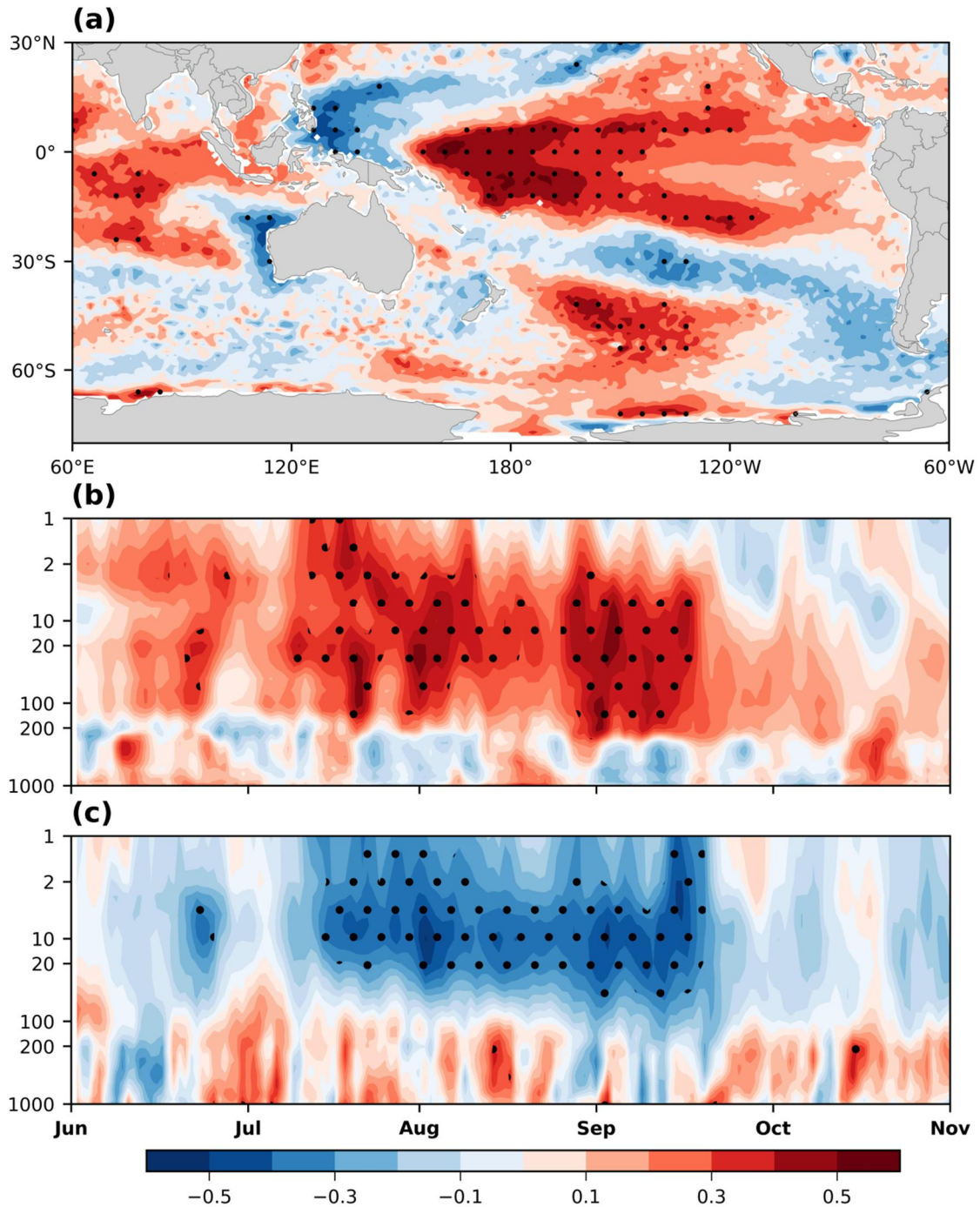
274 **Table 2.** Relationship between ENSO phases in the preceding boreal winter and Antarctic stratospheric  
 275 temperature (AST) anomalies during July–September for the 45-year period (1980–2024).

Year (DJF)	Event Type	AST Anomalies	Year (DJF)	Event Type	AST Anomalies
1980–1981	Neutral	Cold (C)	2002–2003	El Niño (CP)	C
1981–1982	Neutral	C	2003–2004	Neutral	W
1982–1983	El Niño (EP)	C	2004–2005	El Niño (CP)	W
1983–1984	La Niña	Warm(W)	2005–2006	La Niña	C
1984–1985	La Niña	Normal (N)	2006–2007	El Niño (CP)	W
1985–1986	Neutral	W	2007–2008	La Niña	C
1986–1987	El Niño (CP)	C	2008–2009	La Niña	C
1987–1988	El Niño (CP)	W	2009–2010	El Niño (CP)	W
1988–1989	La Niña	C	2010–2011	La Niña	C
1989–1990	Neutral	N	2011–2012	La Niña	W
1990–1991	Neutral	C	2012–2013	Neutral	N
1991–1992	El Niño (CP)	W	2013–2014	Neutral	N
1992–1993	Neutral	N	2014–2015	El Niño (CP)	C
1993–1994	Neutral	N	2015–2016	El Niño (EP)	W
1994–1995	El Niño (CP)	N	2016–2017	La Niña	W
1995–1996	La Niña	W	2017–2018	La Niña	C
1996–1997	Neutral	W	2018–2019	El Niño (CP)	W
1997–1998	El Niño (EP)	C	2019–2020	Neutral	C
1998–1999	La Niña	C	2020–2021	La Niña	C
1999–2000	La Niña	C	2021–2022	La Niña	C
2000–2001	La Niña	C	2022–2023	La Niña	N
2001–2002	Neutral	W	2023–2024	El Niño (EP)	W
El Niño			La Niña		
Total: 14			Total: 17		
Warm (CP) / Cold			Warm / Cold		
8 (6) / 4			4 / 11		
57% / 28.5%			23.5% / 65%		
Neutral			Neutral		
Total: 13			Total: 13		
Warm / Cold			Warm / Cold		
4 / 4			4 / 4		
31% / 31%			31% / 31%		

276

277 Correlation coefficients between the July–September mean  $T_{10-30}$  index and the global SST

278 field from the preceding boreal winter are shown in Figure 1a. The highest correlation coefficients  
 279 are observed in the central Pacific, particularly over the NiñoNiño 4 region. Additionally,  
 280 significant positive correlations appear over the North Indian Ocean and the South Pacific, likely  
 281 reflecting remote responses to ENSO (Alexander et al., 2002).  
 282



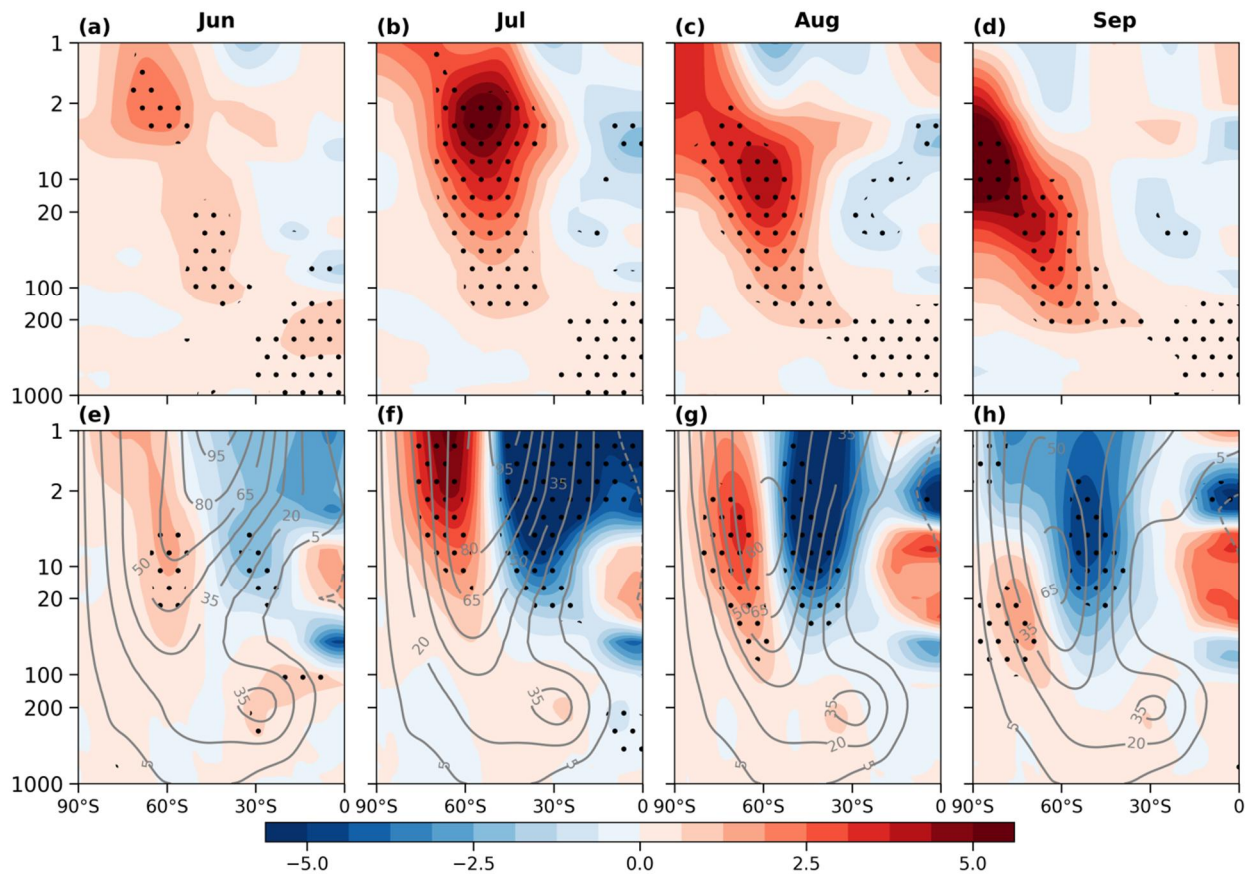
283  
 284 **Figure 1.** (a) Correlation coefficients between July–September mean  $T_{10-30}$  index and January–March mean SST,  
 285 (b) Correlation coefficients between December–February mean NiñoNiño 4 index and daily Temperature

286 averaged over 60 °S–90 °S, and (c) same as (b), but for zonal-mean zonal wind averaged over 40 °S–50 °S. Black  
287 dots represent the 95 % confidence level.

288 The most pronounced impacts of SSTs over the NiñoNiño 4 region occur, however, above 100  
289 hPa during the austral winter of the following year. Figs. 1b-c present the correlations between the  
290 boreal winter NiñoNiño 4 index and the Antarctic daily zonal-mean temperature (averaged over  
291 60 °S–90 °S) and zonal-mean zonal wind (averaged over 40 °S–50 °S) from June to September of  
292 the following year. The NiñoNiño 4 index exhibits significant positive correlations with  
293 stratospheric temperature and negative correlations with zonal wind during July–September,  
294 consistent with the stratospheric warming and weakened SPV.

295 To further examine the impacts of NiñoNiño 4 SST anomalies on the stratospheric  
296 temperatures and the SPV, 17 warm years and 14 cold years according to  $\pm 0.5$  standard of the  
297 NiñoNiño 4 index are selected to calculate composite differences in vertical zonal-mean  
298 temperature and zonal wind (Figs. 2). The  $\pm 0.5$  standard deviation threshold is chosen to capture  
299 relatively strong warm and cold events, but the results are not sensitive to the specific threshold  
300 value. In June, warming is primarily observed in the upper polar stratosphere and the tropical  
301 troposphere, with the strongest signal at 1–5 hPa (Fig. 2a). As the season progresses, the warming  
302 intensifies and gradually propagates downward and poleward, with peak anomalies centered  
303 around ~65 °S in July–August (Figs. 2b–c). This warming reaches its maximum at 10 hPa around  
304 87–90 °S in September (Figs. 2d).

305



306

307 **Figure 2.** Composite differences between warm and cold Niño 4 years for (a,e) June, (b,f) July, (c,g) August, and  
 308 (d,h) September. (a–d) Zonal–mean temperature (shaded, unit: K), and (e–h) zonal–mean zonal winds (shaded,  
 309 unit: m/s), where the climatological mean of zonal-mean zonal wind is computed from 1991–2020 (contour, unit:  
 310 m/s). Black dots indicate regions statistically significant at the 95% confidence level.

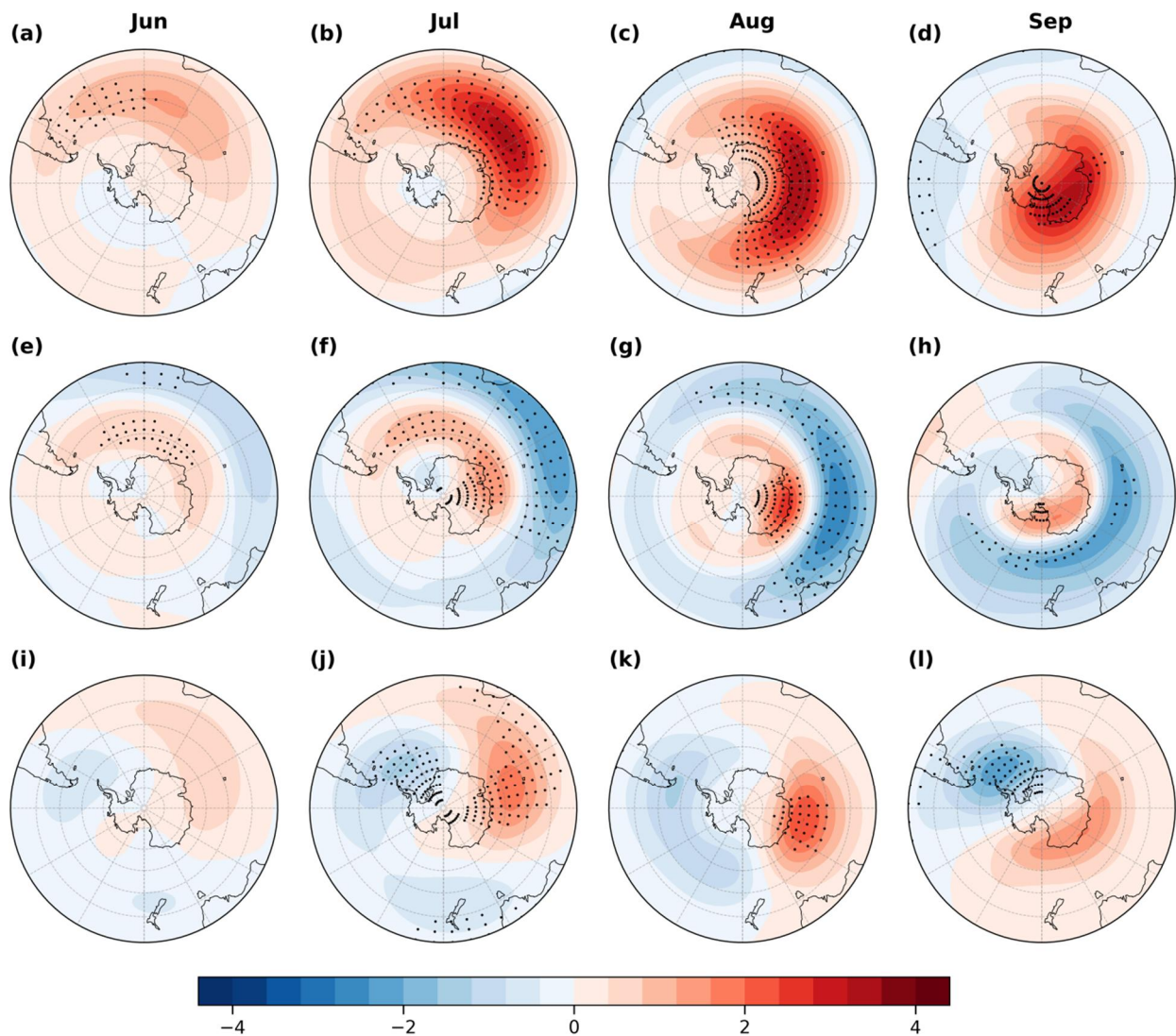
311

312 In general, the stratospheric warming anomalies are accompanied by a significant weakening  
 313 of the polar stratospheric westerlies (Figs. 2e–h). Under climatological conditions, the polar night  
 314 jet typically establishes and strengthens gradually from June to July, centered near 1 hPa and around  
 315 45 °S (Figs. 2e–f). The jet core then migrates poleward and downward in August and weakens in  
 316 September (Figs. 2g–2h). However, during warm NiñoNiño 4 years, anomalous easterlies emerge  
 317 south of 45 °S and anomalous westerlies develop south of 60 °S as early as June (Figs. 2e),  
 318 and while anomalous easterlies progressively shift poleward from July to September, substantially  
 319 weakening the climatological westerlies (Figs. 2f–h), anomalous westerlies develop south of 60 °S,  
 320 indicating a notable poleward contraction and shift of the SPV (Figs. 2f–h). This pattern reflects a  
 321 delayed yet robust stratospheric response to warm SST anomalies in the tropical central Pacific.

322 Moreover, the atmospheric responses exhibit the maximum stratospheric warming appears  
 323 over the Indian Ocean during June–September, while no significant warming is observed in the

324 South Pacific (Fig. 3a-d). This warming pattern tends to weaken midlatitude baroclinicity,  
 325 producing a westerly anomaly at high latitudes and a negative anomaly in the midlatitude in  
 326 stratosphere, indicative of a contraction of the jet stream (Figs. 3e-h). Meanwhile, the stratospheric  
 327 geopotential height show a zonal wavenumber-1 pattern, with a positive center over the Indian  
 328 Ocean and a negative center over the Pacific and Atlantic, suggesting a role of planetary wave (Figs.  
 329 3i-l). The responses intensify from June to September and gradually propagate eastward and  
 330 poleward (Fig. 3). For example, the maximum westerly anomalies extend into the Pacific polar  
 331 region by September, while pronounced negative wind anomalies develop over the midlatitude  
 332 Pacific (Fig. 3h).

333



334

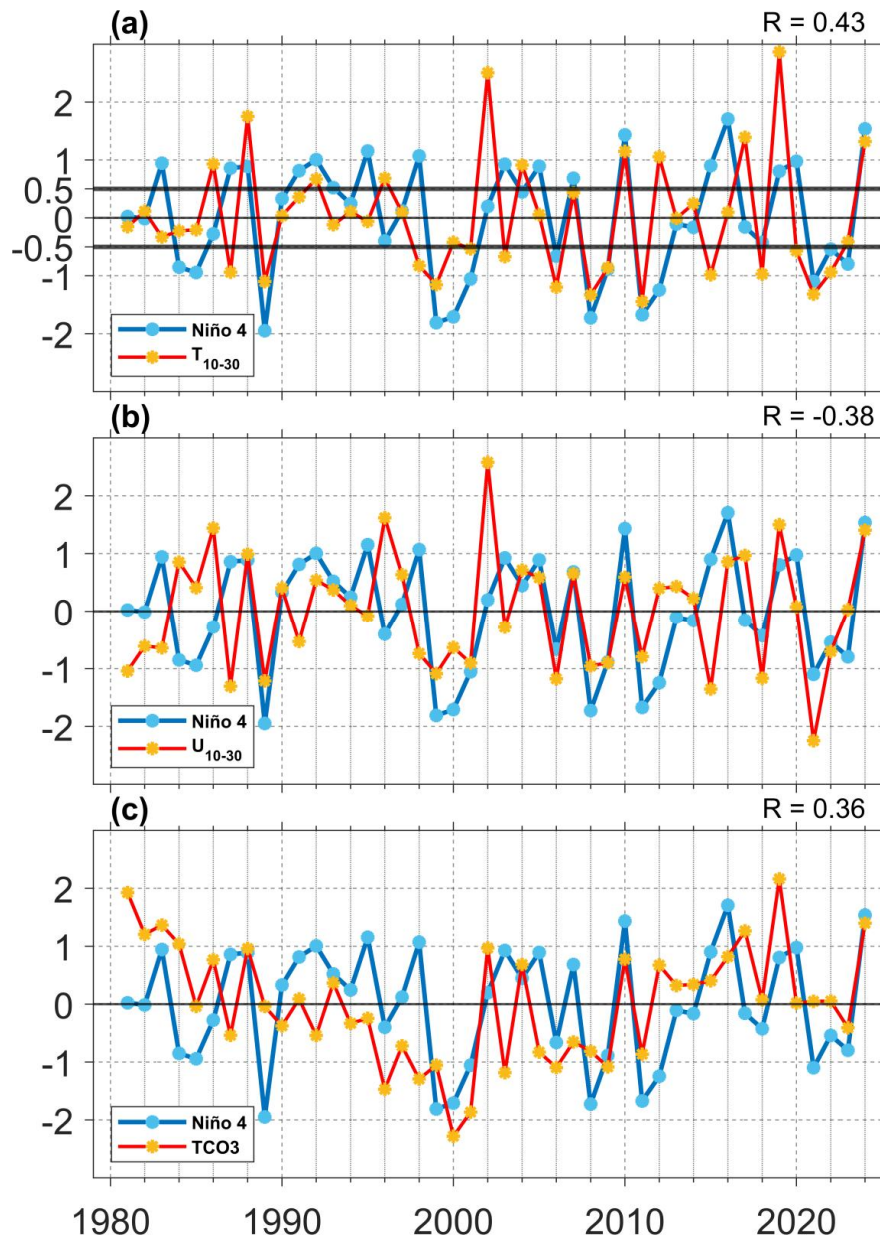
335 **Figure 3.** Composite differences between warm and cold Niño 4 years for (a,e,i) June, (b,f,j) July, (c,g,k) August,  
 336 and (d,h,l) September. (a–d) Temperature averaged over 10–30 hPa (shaded, unit: 2 K), (e–h) zonal wind averaged  
 337 over 10–30 hPa (shaded, unit: 5 m/s), and (i–l) geopotential height averaged over 10–30 hPa (shaded, unit: 10

338 dagpm). Black dots indicate regions statistically significant at the 95% confidence level.

339

340 Figures 34a–b present time series of the boreal winter ~~Niño~~Niño 4 index alongside the July–  
341 September mean  $T_{10-30}$  and  $U_{10-30}$  indices from 1981–2024. The ~~Niño~~Niño 4 index exhibits a  
342 significant positive correlation with the  $T_{10-30}$  index ( $R = 0.43$ ,  $p < 0.01$ ) (~~Fig. 3~~Fig. 4a) and a  
343 significant negative correlation with the  $U_{10-30}$  index ( $R = -0.38$ ,  $p < 0.01$ ) (~~Fig. 3~~Fig. 4b), both are  
344 significant at the 99 % confidence level, indicating that a high (low) ~~Niño~~Niño 4 index is typically  
345 associated with a warmer (colder) polar stratosphere and ~~contractedweaker~~ (~~stronger~~expanded)  
346 SPV. Notably, several prominent sudden stratospheric warming (SSW) events (e.g., 1988, 2019,  
347 2024) coincide with positive ~~Niño~~Niño 4 SSTs (~~Fig. 3~~Fig. 4a). The associated stratospheric changes  
348 also influence Antarctic ozone concentrations (Wang et al., 2025). For instance,  $TCO_3$  shows a  
349 strong positive correlation with both the  $T_{10-30}$  index ( $R = 0.56$ ,  $p < 0.01$ ) and the boreal winter  
350 ~~Niño~~Niño 4 index ( $R = 0.36$ ,  $p < 0.01$ ), both statistically significant at the 99 % confidence level  
351 (~~Fig. 3~~Fig. 4c). This suggests that warm (cold) ~~Niño~~Niño 4 events enhance (suppress) poleward  
352 ozone transport, thereby increasing (decreasing) ozone concentrations over Antarctica.

353



354

355 **Figure 34.** Time series of standardized NiñoNiño 4 index (blue line), along with (a) July–September mean  $T_{10-30}$   
 356 index (red line), (b) July–September mean  $U_{10-30}$  index (red line, multiplied by -1), and (c) July–September mean  
 357  $TCO_3$  index (red line) from 1981 to 2024. R in the upper right corner denotes the correlation coefficient between  
 358 the NiñoNiño 4 index and the  $T_{10-30}$ ,  $U_{10-30}$ , and  $TCO_3$  indices, respectively.

359

## 360 4 Effects of anomalous planetary waves

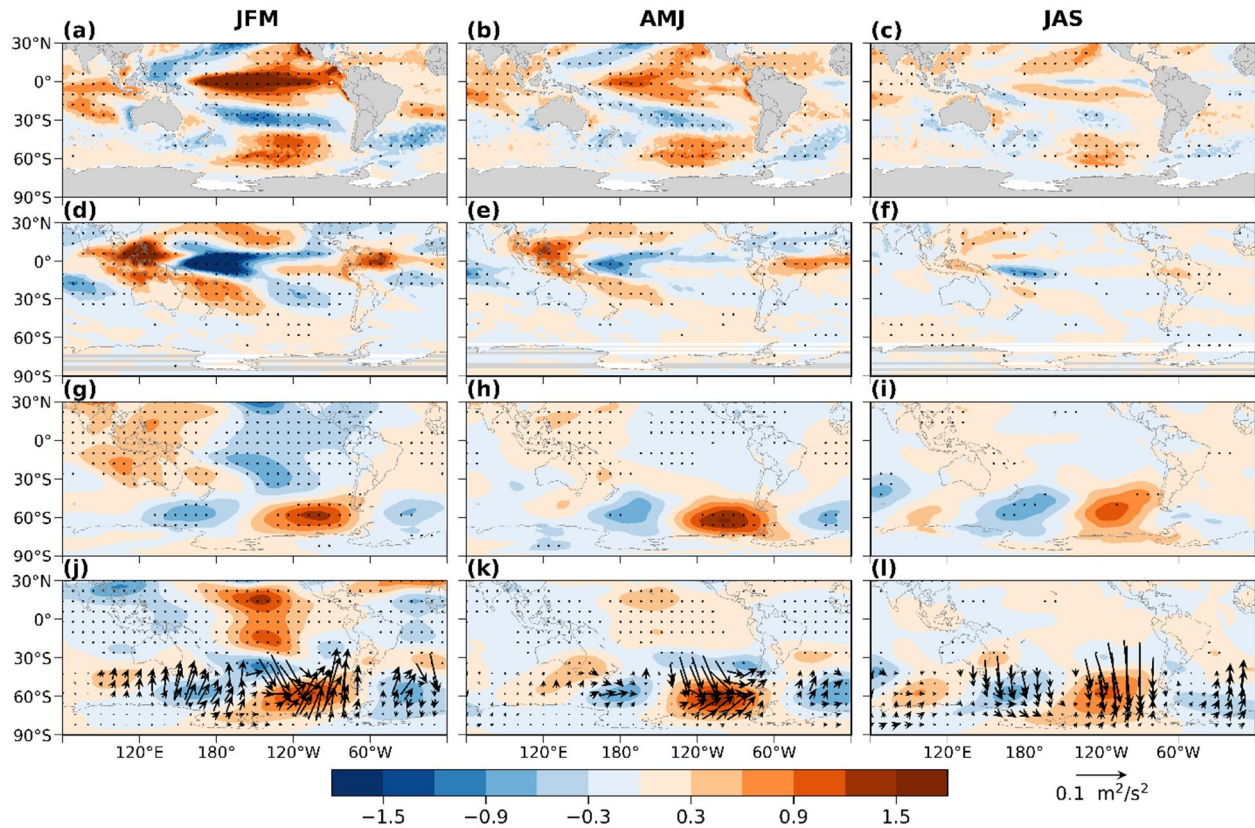
### 361 4.1 Stratospheric temperature and zonal wind

362 Previous studies suggested that polar stratospheric warming is primarily driven by the upward  
 363 propagation of planetary waves from the troposphere, which disturb the SPV through wave–mean  
 364 flow interactions (Baldwin et al., 2021). To evaluate the effect of planetary wave activity on  
 365 Antarctic stratospheric temperature anomalies during different NiñoNiño 4 SST events, the

366 composite differences of key atmospheric variables were calculated between warm and cold  
367 ~~NiñoNiño~~ 4 years, averaged over consecutive three-month periods from January to September of  
368 the following year.

369 During the mature phase of El Niño (January–March), positive SST anomalies develop in the  
370 central and eastern Pacific (~~Fig. 4~~[Fig. 5a](#)). As SST increases, ~~cumulus~~ convection intensifies in the  
371 central Pacific (~~Fig. 4~~[Fig. 5d](#)), accompanied by a negative SLP anomaly and a positive geopotential  
372 height anomaly at 250 hPa over the tropical central Pacific, indicating a barotropic response (~~Figs.~~  
373 ~~4~~[Figs. 5g,j](#)). Furthermore, the convection anomaly triggers a southward-propagating  
374 teleconnection wave train at 250hPa, as suggested by the TN01 flux (Vector, ~~Fig. 4~~[Fig. 5j](#)). This  
375 wave train, known as the PSA teleconnection (Mo and Higgins, 1998), features a positive  
376 geopotential height anomaly over the southeastern Pacific (near 110 °W, 60 °S) and a negative  
377 anomaly over the southwestern Pacific (near 150 °W, 40 °S) (~~Fig. 4~~[Fig. 5j](#)). The warm ~~NiñoNiño~~  
378 4 SSTs and their associated convection responses over the tropical central Pacific persist into April–  
379 June (~~Figs. 4~~[Figs. 5b,e,h,k](#)). Although the amplitude of the high and low-pressure centers over the  
380 southeastern and southwestern Pacific weakens, the PSA wave train remains active (~~Fig. 4~~[Fig. 5k](#)).  
381 By July–September (austral winter), the warm ~~NiñoNiño~~ 4 SSTs and their associated barotropic  
382 responses begin to dissipate (~~Figs. 4~~[Figs. 5c,i,l](#)). However, despite the weakening of tropical  
383 convection (~~Fig. 4~~[Fig. 5f](#)), it is strong enough to sustain a weak mid-latitude PSA wave train,  
384 maintaining a persistent positive geopotential height anomaly over the southeastern Pacific and a  
385 negative anomaly over the South Atlantic, as indicated by the TN01 flux (~~Fig. 4~~[Fig. 5l](#)).

386



387

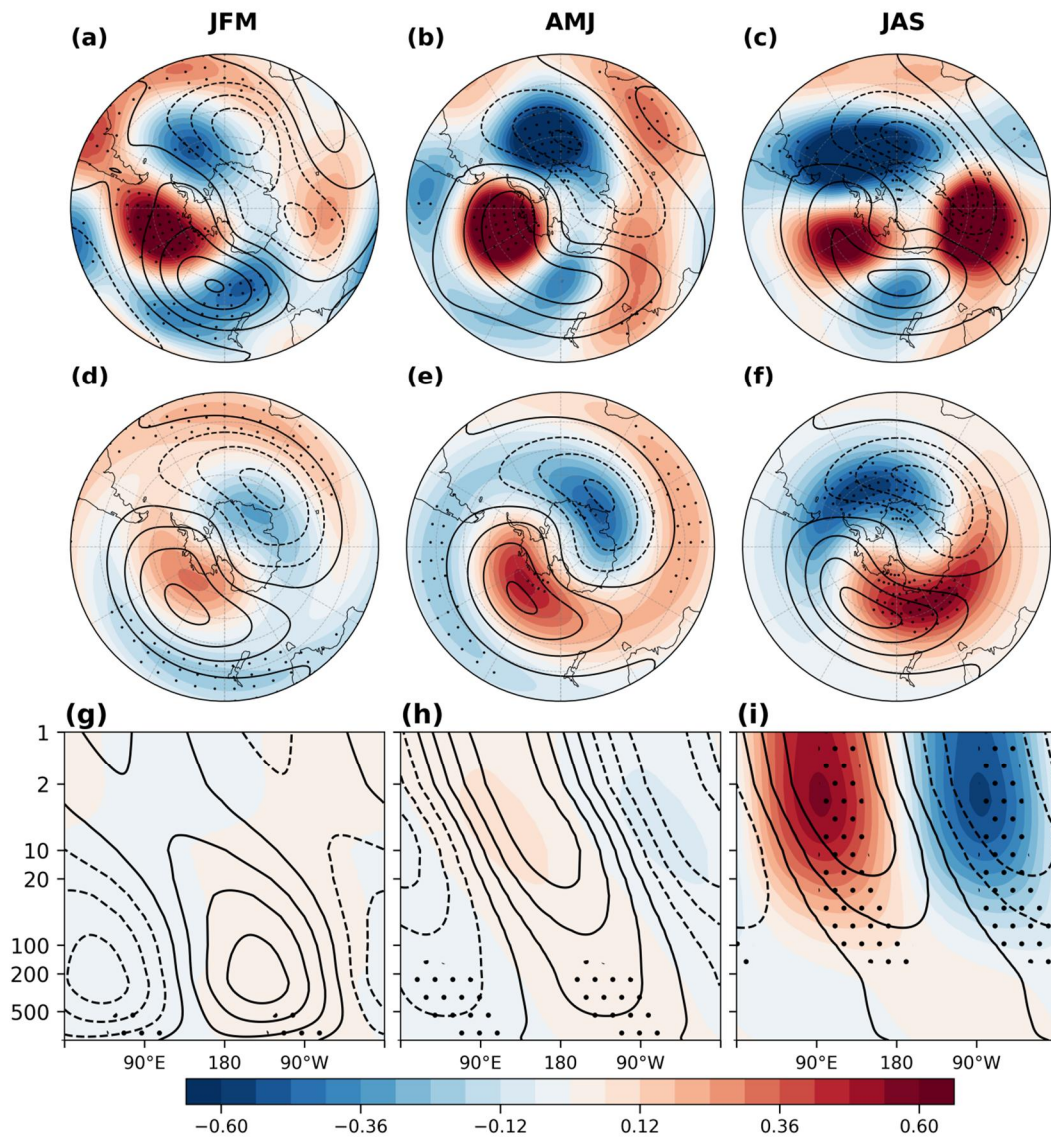
388 **Figure 5.** Composite differences between warm and cold Niño 4 years. The panels show three-month means for  
 389 January–March (left column), April–June (middle column), and July–September (right column). (a–c) Sea  
 390 surface temperature (SST, shaded, unit: K), (d–f) outgoing longwave radiation (OLR, shaded, unit:  $1.5 \times 10^6$   
 391  $\text{W/m}^2$ ), (g–i) sea level pressure (SLP, shaded, unit: 300 Pa), (j–l) Geopotential heights (shaded, unit: 5 dagpm)  
 392 and TN01 flux (vector, unit:  $0.1 \text{ m}^2/\text{s}^2$ ) at 250 hPa. Black dots indicate regions statistically significant at the 95%  
 393 confidence level.

394

395 The geopotential height anomaly extends into the lower stratosphere and remains statistically  
 396 significant at 100 hPa (Fig. 5Fig. 6). The climatological geopotential height at 100 hPa is  
 397 characterized by a wave-1 pattern, featuring a positive center over the South Pacific and a negative  
 398 center over the Atlantic Ocean and Indian Ocean sectors (contour lines in Fig. 5Fig. 6). During  
 399 January–February–March (JFM) (austral summer), geopotential height anomalies associated with  
 400 warm central Pacific SSTs form a wave train, with a positive center over the southeastern Pacific  
 401 and two negative centers over the southwestern Pacific and the southern Atlantic (Fig. 5Fig. 6a).  
 402 However, this pattern does not align well with the climatological wave-1 structure, indicating a  
 403 displacement of the wave pattern (Fig. 5Fig. 6d). Moreover, the anomalous wave-1 centers at high  
 404 latitudes are not statistically significant (Fig. 5Fig. 6d). Although the wave-1 component of the  
 405 geopotential height shows a westward tilt with altitude and broadly resembles with the

406 climatological structure, this alignment is only statistically significant below 500 hPa (Fig. 5 Fig.  
 407 6g). As a result, planetary waves are not substantially amplified in the lower stratosphere, primarily  
 408 due to the prevailing easterly winds in the upper stratosphere over Antarctica in JFM (contours,  
 409 Fig. 6 Fig. 7a), which inhibit upward propagation of planetary waves (Baldwin et al., 2021). This is  
 410 further supported by the E–P flux vectors, which show that planetary wave propagation is largely  
 411 confined below 50 hPa in the mid- and low-latitudes (Fig. 6 Fig. 7a).

412



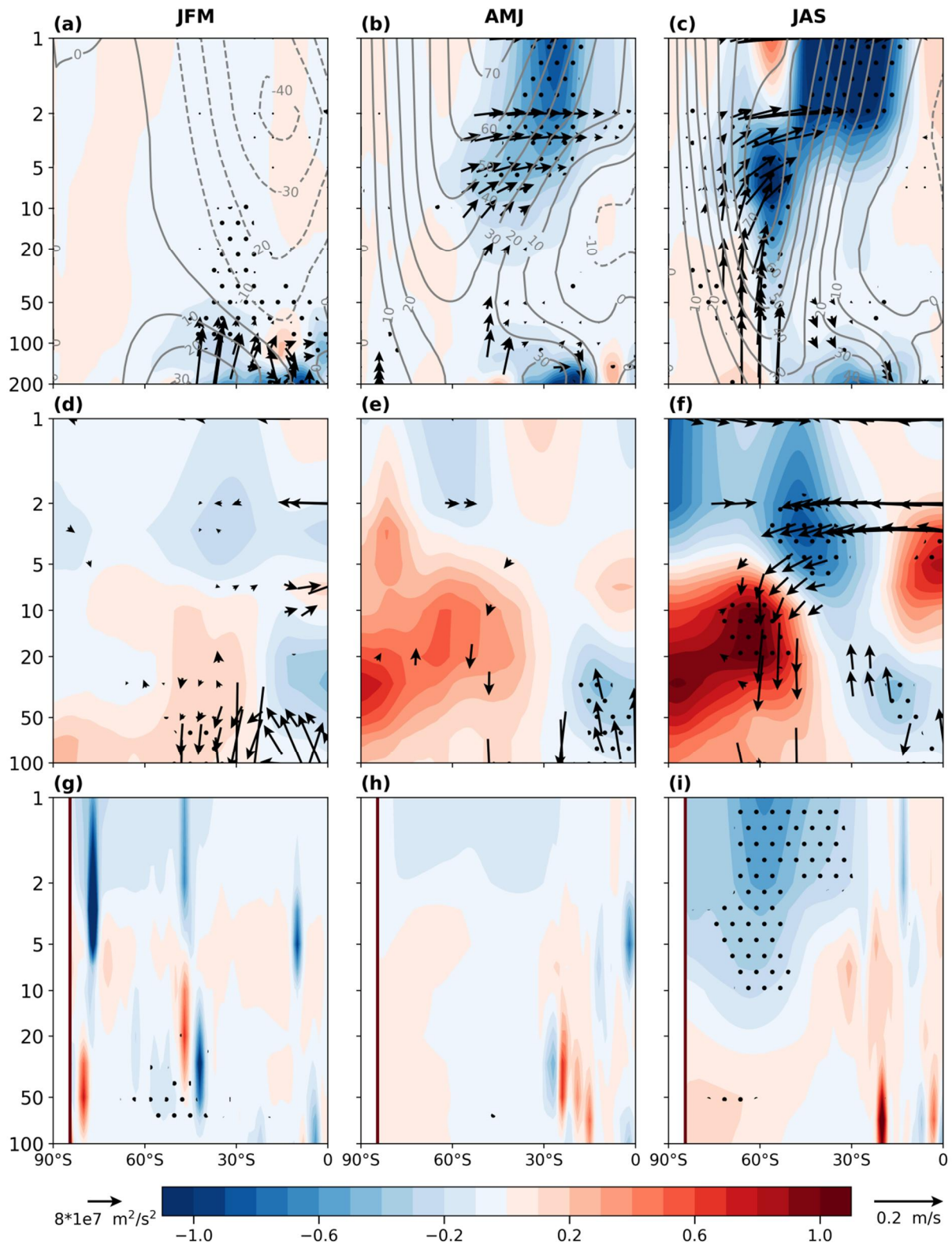
413

414 **Figure 6.** Composite differences between warm and cold Niño 4 years. The panels show three-month means for  
 415 January–March (left column), April–June (middle column), and July–September (right column). (a–c)  
 416 Geopotential heights at 100 hPa (shaded, unit: 5 dagpm), (d–f) wave-1 of geopotential heights at 100 hPa (shaded,  
 417 unit: 5 dagpm), and (g–i) wave-1 of geopotential heights averaged over 45°S–75°S at 1000–1 hPa (shaded, unit:  
 418 30 dagpm). The climatological geopotential height is calculated from 1991–2020 (contours, unit: dagpm). Black  
 419 dots indicate regions statistically significant at the 95% confidence level.

420

421 During April-May-June (AMJ), the positive geopotential height center over the southeastern  
422 Pacific and the negative center over the southern Atlantic become more pronounced (~~Fig. 5~~Fig. 6b),  
423 aligning more closely with the climatological wave-1 pattern (~~Fig. 5~~Fig. 6e). This alignment  
424 contributes to a westward tilt of the geopotential height field with altitude (~~Fig. 5~~Fig. 6h). However,  
425 this vertical tilt is only statistically significant below 100 hPa (~~Fig. 5~~Fig. 6h). During this period,  
426 stratospheric zonal winds gradually transition to a westerly regime, but large portions of the upper  
427 polar stratosphere continue to experience weak westerlies or even easterlies (contours, ~~Fig. 6~~Fig.  
428 7b). As a result, a significant portion of the planetary waves are refracted equatorward, and their  
429 ability to disturb the polar stratosphere remains limited (~~Fig. 6~~Fig. 7b).

430



431

432 **Figure 7.** Composite differences between warm and cold Niño 4 years. The panels show three-month means for  
 433 January–March (left column), April–June (middle column), and July–September (right column). (a–c) E–P flux  
 434 (vector:  $\text{m}^2/\text{s}^2$ ) and its divergence (shaded, unit:  $60 \text{ m/s/day}$ ), where the climatological zonal-mean zonal wind  
 435 are calculated from 1991–2020 (contours, unit:  $\text{m/s}$ ), (d–f) ozone mass mixing ratio (shaded, unit:  $3 \times 10^{-6} \text{ kg/kg}$ )  
 436 and residual mean circulation (vector, unit:  $\text{m/s}$ ), and (g–i) wave reflective index (shaded, unit: %). Black dots  
 437 indicate regions statistically significant at the 95% confidence level.

438

439 –During July-August-September (JAS), the geopotential height centers over the southeastern  
 440 Pacific weaken, while the positive center over the southern Indian Ocean strengthens significantly  
 441 (~~Fig. 5~~Fig. 6c). This spatial pattern enhances the climatological wave-1 trough and ridge structure  
 442 (~~Fig. 5~~Fig. 6f) and exhibits a westward tilt of the geopotential height field with altitude, which  
 443 becomes statistically significant in the stratosphere (~~Fig. 5~~Fig. 6i). Although the wave-2 pattern  
 444 exhibits a strong amplitude, it is nearly orthogonal to the climatological wave-2 phase during July–  
 445 September. Therefore, the wave-2 component is not reinforced, and the process is mainly  
 446 dominated by the wave-1 pattern (Figures not shown). During this period, the polar regions enter  
 447 the polar night, with minimal solar heating, which increases baroclinicity in the mid- and high-  
 448 latitudes. The stratosphere becomes fully dominated by strong westerly winds, creating favorable  
 449 conditions for the upward propagation of planetary waves into the polar stratosphere (contour lines,  
 450 ~~Fig. 6~~Fig. 7c). In addition, the wave reflection index exhibits a significant negative anomaly south  
 451 of 30 °S in the upper stratosphere (Fig. 7i). This further indicates that planetary waves are strongly  
 452 refracted toward the mid- and high-latitude stratosphere (Fig. 7c). Based on the E–P flux theorem  
 453 (Matusno, 1971), when E–P flux convergence occurs in the midlatitudes, the jet stream tends to  
 454 weaken and poleward heat transport increases. During July–September, the strong Antarctic polar  
 455 vortex inhibits the poleward propagation of planetary waves, resulting in relatively weak polar  
 456 warming and stronger warming in the subpolar and midlatitude regions. As a result, significant  
 457 high-latitude warming and contraction of the polar vortex are observed during April–September  
 458 (Fig 3).

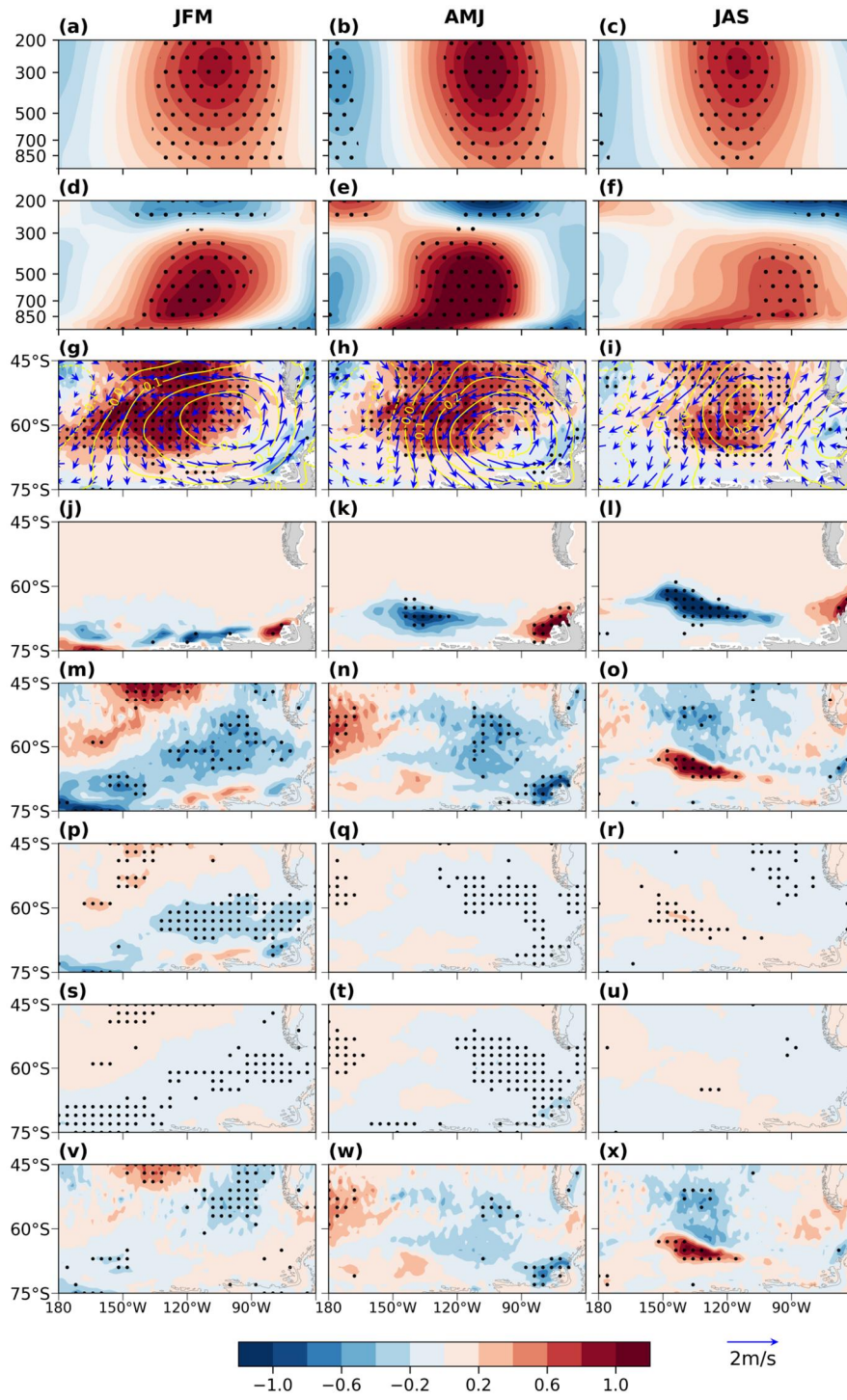
459 This relationship is reversed under cold ~~Niño~~Niño 4 SST conditions. Specifically, when cold  
 460 SST anomalies occur in the central tropical Pacific, planetary wave activity and their associated  
 461 disturbances to the stratosphere are suppressed, leading to polar stratospheric cooling and a  
 462 strengthening SPV.

## 463 4.2 Mid-latitude sea-air interactions

### 464 4.2.1 Ocean responses

465 ~~Niño~~Niño 4 SSTs influence mid-latitude ocean temperatures through atmospheric  
 466 teleconnections. During JFM, a positive ~~Niño~~Niño 4 SSTs trigger a PSA teleconnection pattern,

467 resulting in a high-pressure anomaly centered near 110 °W, 60 °S over the southeastern Pacific  
468 (~~Figs. 4~~Figs. 5j and 7g). The associated poleward surface winds and adiabatic subsidence warm the  
469 lower troposphere (~~Figs. 7~~Figs. 8a,d), while the ocean gains heat, as indicated by the negative net  
470 heat flux anomaly, defined as the sum of latent and sensible heat fluxes, long-wave radiant and  
471 short-wave radiant heating (~~Fig. 7~~Fig. 8m), leading to a localized SST warming (~~Fig. 7~~Fig. 8g).  
472 Simultaneously, there is a modest reduction in SIC in the Amundsen and Ross Seas (~~Fig. 7~~Fig. 8j).  
473



474

475 **Figure 8.** Composite differences between warm and cold Niño 4 years. The panels show three-month means for  
 476 January–March (left column), April–June (middle column), and July–September (right column). (a–c)  
 477 Geopotential heights (shaded, unit: 5 dagpm), averaged over 45°S–75°S, (d–f) temperatures (shaded, unit: K),  
 478 averaged over 45°S–75°S, (g–i) SST (shaded, unit: K), SLP (contours, unit: 1000 Pa), and 10-meter winds  
 479 (vector, unit: 2 m/s), (j–l) sea ice concentration (SIC, unit: 100 %), (m–o) net upward total heat flux (the sum of  
 480 turbulence heat flux, upward long-wave heat flux and net downward short-wave radiation, shaded, unit: 3 W/m<sup>2</sup>),  
 481 (p–r) net downward short-wave radiation (shaded, unit: 3 W/m<sup>2</sup>), (s–u) upward long-wave radiation (shaded, unit:  
 482 3 W/m<sup>2</sup>), and (v–x) turbulence heat flux (the sum of latent and sensible heat flux; shaded, unit: 3 W/m<sup>2</sup>). Black  
 483 dots indicate regions statistically significant at the 95% confidence level.

484

485 A similar pattern persists during AMJ (Figs. 7Figs. 8b,e). The PSA pattern associated with  
 486 warm NiñoNiño 4 SSTs remains evident (Fig. 4Fig. 5k), although the area of negative net heat flux  
 487 contracts (Fig. 7Fig. 8n), and continues to support elevated SSTs in the southeastern Pacific through  
 488 ongoing sea-air heat exchange (Fig. 7Fig. 8h). As a result, SIC in the Amundsen and the Ross Seas  
 489 declines further (Fig. 7Fig. 8k). Additionally, sustained tropospheric warming enhances  
 490 geopotential height anomalies in both the troposphere and lower stratosphere (Figs. 7Figs. 8b,e).

#### 491 4.2.2 Ocean feedback to the atmosphere

492 While the tropospheric warming center is located between 500 hPa and 850 hPa during JFM  
 493 and AMJ, the maximum warming shifts below 850 hPa in JAS, suggesting an increased influence  
 494 from the ocean surface (Figs. 7Figs. 8d-f). During the JAS, the NiñoNiño 4 SST warming weakens  
 495 (Fig. 4Fig. 5c), indicating a reduced influence of equatorial central-Pacific SSTs. Nevertheless, due  
 496 to the ocean's large heat capacity, warm SSTs in the southeastern Pacific persist (Fig. 7Fig. 8i),  
 497 although with reduced amplitude, implying that the accumulated heat is gradually being released  
 498 (Fig. 7Fig. 8o). A pronounced positive geopotential height anomaly associated with the PSA pattern  
 499 also remains over this region (Fig. 4Fig. 5l), likely sustained by local sea-air interactions.

500 In JAS, surface net heat flux is largely associated with sea-ice loss in the Amundsen and Ross  
 501 Seas (Figs. 7Figs. 8l,o). Specifically, the sustained warm SSTs drive substantial sea-ice loss, ~~which~~  
 502 ~~reduces surface albedo and enhances short-wave radiation absorption, further accelerating sea-ice~~  
 503 ~~decline. Comparison between surface heat flux (Fig.8o) and ice concentration (Fig.8l) shows ice~~  
 504 ~~loss has a pronounced impacts on surface heat flux. During JAS, solar short-wave radiation reaches~~  
 505 ~~its minimum, and its contribution to the net heat flux is relatively small. (Fig. 8r). The primary~~  
 506 ~~contributions come from turbulence heat fluxes (Fig. 8x) and temperature advection (Fig 8i), while~~  
 507 ~~the contribution from longwave radiation is relatively weak (Fig. 8u). During this stage, southerly~~  
 508 ~~anomalies dominate the region over 40°–60°S, 90°–140°W, which transport warm air from tropical~~  
 509 ~~regions to the midlatitudes and enhance ocean heat uptake from atmosphere. Although~~ the negative  
 510 net heat flux anomalies persist north of 60 °S, their intensity is relatively weak. In contrast,  
 511 significant oceanic heat is released to the atmosphere in the regions where sea-ice has retreated  
 512 (Fig. 7Fig. 8o), warming the lower troposphere (Fig. 7Fig. 8f) and sustaining the positive  
 513 geopotential height anomaly by lifting isobaric surfaces (Fig. 7Fig. 8c). Notably, while net heat

514 flux is dominated by ocean heat uptake during JFM and AMJ, the influence of sea-ice loss becomes  
515 predominant in JAS, resulting in net heat release from the ocean to the atmosphere (Figs. 7Figs.  
516 8m-o). This positive feedback reinforces the Southern Hemisphere zonal-wave pattern and  
517 amplifies the planetary wave anomalies (Zi et al., 2025). Recent modeling studies also suggest that  
518 sea ice loss in the Amundsen Sea and the broader Antarctic region can have pronounced impacts  
519 on stratospheric polar vortex (Song et al., 2025). The loss of sea ice tends to sustain the influence  
520 of Niño 4 SST on stratospheric temperatures during JAS by enhancing surface heat fluxes (Fig.8).

### 521 4.3 Ozone transport

522 The enhanced planetary wave activity associated with the ~~Niño~~Niño 4 SST warming not only  
523 warms the polar stratosphere but also significantly alters the B–D residual circulation and polar  
524 ozone transport (Wang et al., 2025). Figures 67d–67f present the composite differences in the zonal-  
525 mean residual circulation and ozone mass mixing ratio between warm and cold ~~Niño~~Niño 4 years,  
526 each averaged over three–month periods from January to September of the following year.

527 During JFM, convective anomalies in the tropical Pacific Ocean drive changes in the residual  
528 circulation (Fig. 4Fig. 5d), resulting in decreases to the ozone mass mixing ratio in the tropical  
529 lower stratosphere and increased values in the mid–latitude lower stratosphere (Fig. 6Fig. 7d).  
530 However, upward–propagating planetary waves are largely confined below 50 hPa in the mid– and  
531 low–latitudes (Fig. 6Fig. 7a), strengthening the residual circulation primarily north of 60 °S. As a  
532 result, ozone transport to higher altitudes and into the polar region remains limited (Fig. 6Fig. 7d).  
533 In AMJ, although convective anomalies in the tropical Pacific Ocean persist and wave activity  
534 increases in the upper stratosphere (Fig. 6Fig. 7b), many of the waves are refracted equatorward,  
535 resulting in only modest polar ozone transport (Fig. 6Fig. 7e). In JAS, however, upward–  
536 propagating planetary waves are strongly refracted toward mid– and high–latitudes, enhancing the  
537 residual circulation and promoting both poleward and upward ozone transport (Fig. 6Fig. 7f). The  
538 increased poleward ozone transport enhances solar radiation absorption, playing an important role  
539 in the polar stratospheric warming through dynamical–chemical coupling (Solomon et al., 2016).  
540 In addition, adiabatic warming associated with descending air in the residual circulation further  
541 contributes to the stratospheric warming over the polar region.

542

## 543 5 Multivariate regression model

544 Nino 4 SST anomalies can influence stratospheric temperatures through the PSA pattern,  
 545 which affects surface conditions at high latitudes during boreal winter. During JAS, the atmospheric  
 546 circulation associated with the PSA pattern can enhance surface heat transport (Fig. 8i) and help  
 547 sustain the stratospheric response (Figs. 8c, f).

548 The preceding analyses reveal that boreal winter ~~Niño~~Niño 4 SSTs exert a significant lagged  
 549 influence on the Antarctic stratospheric circulation ~~and ozone transport~~ during the subsequent  
 550 austral winter. This finding has important implications for the seasonal prediction of stratospheric  
 551 variability. However, although the boreal winter ~~Niño~~Niño 4 index is significantly correlated with  
 552 July–September mean  $T_{10-30}$  index, it accounts for only 18.5 % of the variance in stratospheric  
 553 temperature ( $R^2 = 0.185$ ). To more interpret variability in the Antarctic stratosphere, additional  
 554 factors need to be considered.

555 Previous studies found that ~~the~~the PSA teleconnection associated with ~~Niño~~Niño 4 SSTs is a  
 556 key mechanism influencing the Antarctic stratosphere. The PSA pattern is represented by the  
 557 second EOF mode of monthly SLP anomalies (~~Fig. 8~~Fig. 9). The corresponding PSA index is  
 558 defined as the time series of this EOF mode. During boreal winter, the PSA index is significantly  
 559 correlated with the ~~Niño~~Niño 4 index ( $R = 0.40$ ,  $p < 0.01$ ), suggesting that ~~Niño~~Niño 4 SSTs  
 560 modulate the PSA pattern. However, the correlation between the June PSA index and the Niño 4  
 561 index is not significant ( $r = 0.28$ ,  $p > 0.05$ ). In addition , the June PSA index is significantly  
 562 correlated with Antarctic sea ice ( $r = 0.49$ ,  $p < 0.01$ ), suggesting that the June PSA pattern may be  
 563 maintained by sea ice anomalies and another factors. Furthermore, correlating the PSA index from  
 564 December to the following September with the July–September mean  $T_{10-30}$  index shows that the  
 565 June PSA index exhibits the strongest correlation (Table 3,  $R = 0.47$ ,  $p < 0.01$ ). Interestingly, the  
 566 June PSA index is only moderately correlated with the winter ~~Niño~~Niño 4 index ( $R = 0.28$ ,  $p \geq$   
 567 0.405), indicating that it partially captures independent variability.

568

569

570

571

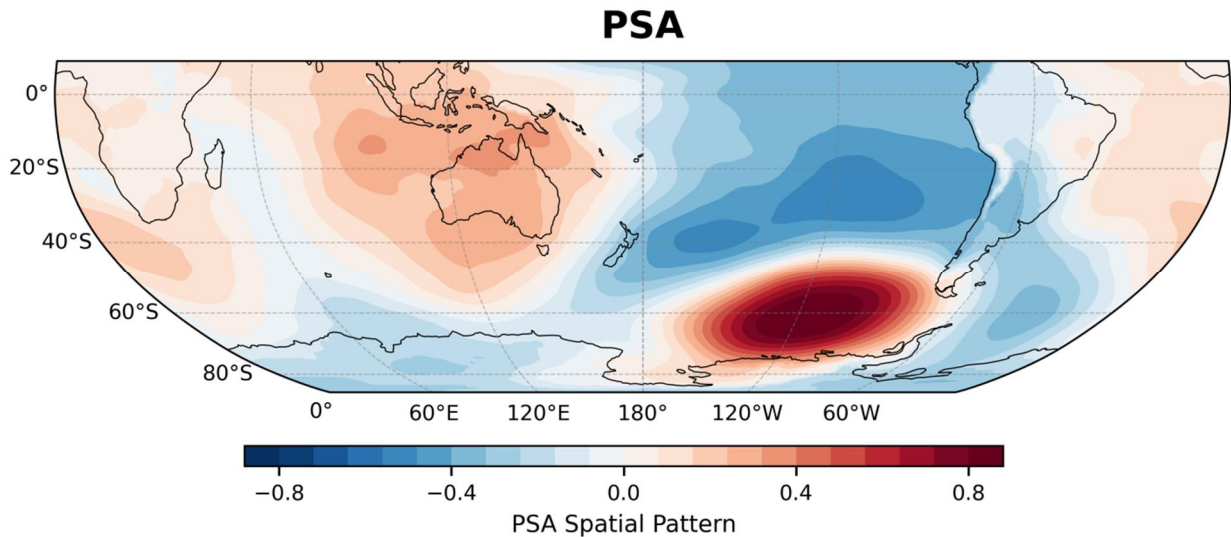
572

573 **Table 3.** Correlation coefficients between sea ice concentration indices ( $SIC_{AR}$ ) over the Amundsen and Ross  
 574 Seas (averaged over  $180^{\circ}W-90^{\circ}W$ ), sea surface temperature indices over the South Pacific ( $SST_{SP}$ ) and Pacific–  
 575 South America teleconnection (PSA) and July–September mean zonal-mean temperature index ( $T_{10-30}$ ) averaged  
 576 over  $60^{\circ}S$  to  $90^{\circ}S$ .

	$SIC_{AR}$	$SST_{SP}$	PSA
Jan	-0.18	0.25	0.32**
Feb	-0.08	0.27*	0.21
Mar	-0.18	0.29*	0.28*
Apr	-0.24	0.30**	-0.12
May	-0.38***	0.27*	0.10
Jun	-0.44***	0.32**	0.47***
Jul	-0.23	0.30**	0.03
Aug	-0.28*	0.30**	0.29*
Sep	-0.31**	0.29*	0.05

577 Note: Colors and asterisks denote statistical significance: red with \*\*\* for the 99 % confidence level, green  
 578 with \*\* for 95 %, and magenta with \* for 90 %.

579



580

581 **Figure 9.** PSA teleconnection pattern represented by the second EOF mode of monthly SLP.

582

583 As a result, a multivariate linear regression (MLR) model is used to quantitatively assess the  
 584 linear relationship between the stratospheric temperature index ( $T_{10-30}$ ) and potential predifactors  
 585 including the NiñoNiño 4 index, and PSA index, South Pacific SST index ( $SST_{SP}$ ), and SIC index.

586 We have

$$587 T_{10-30} = \beta_0 + \beta_1 Niño4 + \beta_2 PSA + \beta_3 SST_{SP} + \beta_4 SIC + \varepsilon \quad (7)$$

588 where  $\beta_0$  is the intercept,  $\beta_1, \beta_2, \beta_3, \beta_4$  are the regression coefficients associated with  
 589 each predifactor, and  $\varepsilon$  denotes the residual error term. Prior to the regression analysis based on

Eq. (7), all input time series are standardized. The regression analysis is performed using MATLAB's fitlm function, which yields estimates of regression coefficients, standard errors, t-statistics, and p-values, along with overall model diagnostics, such as the coefficient of determination ( $R^2$ ) and the F-statistic. To evaluate the significance of individual predifactors, three confidence levels are adopted: 90 %, 95 %, and 99 %, corresponding to p-value thresholds of 0.1, 0.05, and 0.01, respectively. Predifactors with p-values below these thresholds are considered statistically significant. The overall performance and goodness-of-fit of the model are assessed using the  $R^2$  metric.

To predict the July–September mean  $T_{10-30}$  index, the boreal winter NiñoNiño 4 (NiñoNiño 4<sub>DJF</sub>) index, and the June PSA ( $PSA_{Jun}$ ) index, ~~the June  $SST_{SP}$  ( $SST_{SP_{Jun}}$ ) index, and the May–June mean SIC ( $SIC_{MJ}$ ) index~~ are used as predifactors in Eq. (7). We yield

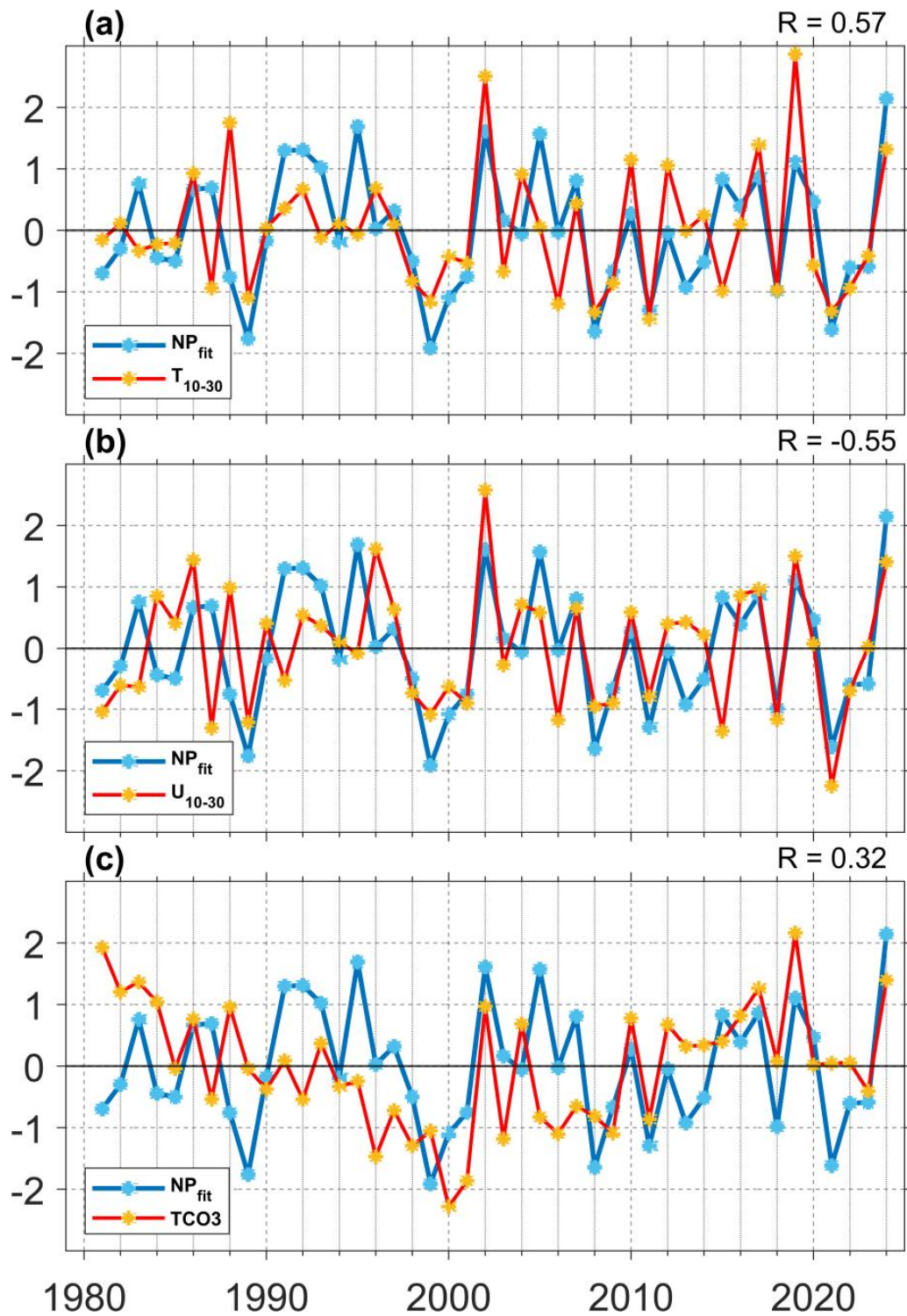
$$T_{10-30} = 0.2765324 Niño4_{DJF} + 0.2879384 PSA_{Jun} + 0.1176 SST_{SP_{Jun}} - 0.1347 SIC_{MJ} + \varepsilon \quad (8)$$

with  $\beta_0 = 0$ . This ~~four-variable~~ linear regression model yields a coefficient of determination ( $R^2$ ) of 0.3521, indicating that the predifactors collectively explain approximately 35.2 % of the variance in the July–September mean  $T_{10-30}$  index. The model's F-statistic is 5.249.71 with a corresponding p-value of 0.000350.00178, which is significant at the 99 % confidence level.

Among the predifactors, NiñoNiño 4<sub>DJF</sub> and  $PSA_{Jun}$  exhibit statistically significant regression coefficients ( $p = 0.0201$  and  $p = 0.0065$ , respectively), confirming their primary roles in modulating stratospheric temperature.

To assess model performance, the regression-based fitted index (referred to as  $NP_{fit}$ ) was compared with observed July–September mean  $T_{10-30}$ ,  $U_{10-30}$ , and  $TCO_3$  (~~Fig. 9~~Fig. 10). The  $NP_{fit}$  index shows significant correlation with observed values for  $T_{10-30}$  ( $R = 0.597$ ,  $p < 0.01$ ),  $U_{10-30}$  ( $R = -0.565$ ,  $p < 0.01$ ), and  $TCO_3$  ( $R = 0.392$ ,  $p < 0.045$ ), all of which exceed the corresponding correlation values ( $R = 0.4$ ,  $-0.38$  and  $0.36$ ) obtained using NiñoNiño 4 index alone (Fig. 2). While the boreal winter Niño 4 index plays a key role in Antarctic stratospheric temperature variability, incorporating the June PSA index further improves the explanation of this variability. This underscores the importance of both tropical forcing and extratropical feedback processes in modulating polar stratospheric circulation.

619



620

621

622

623

624

625

626

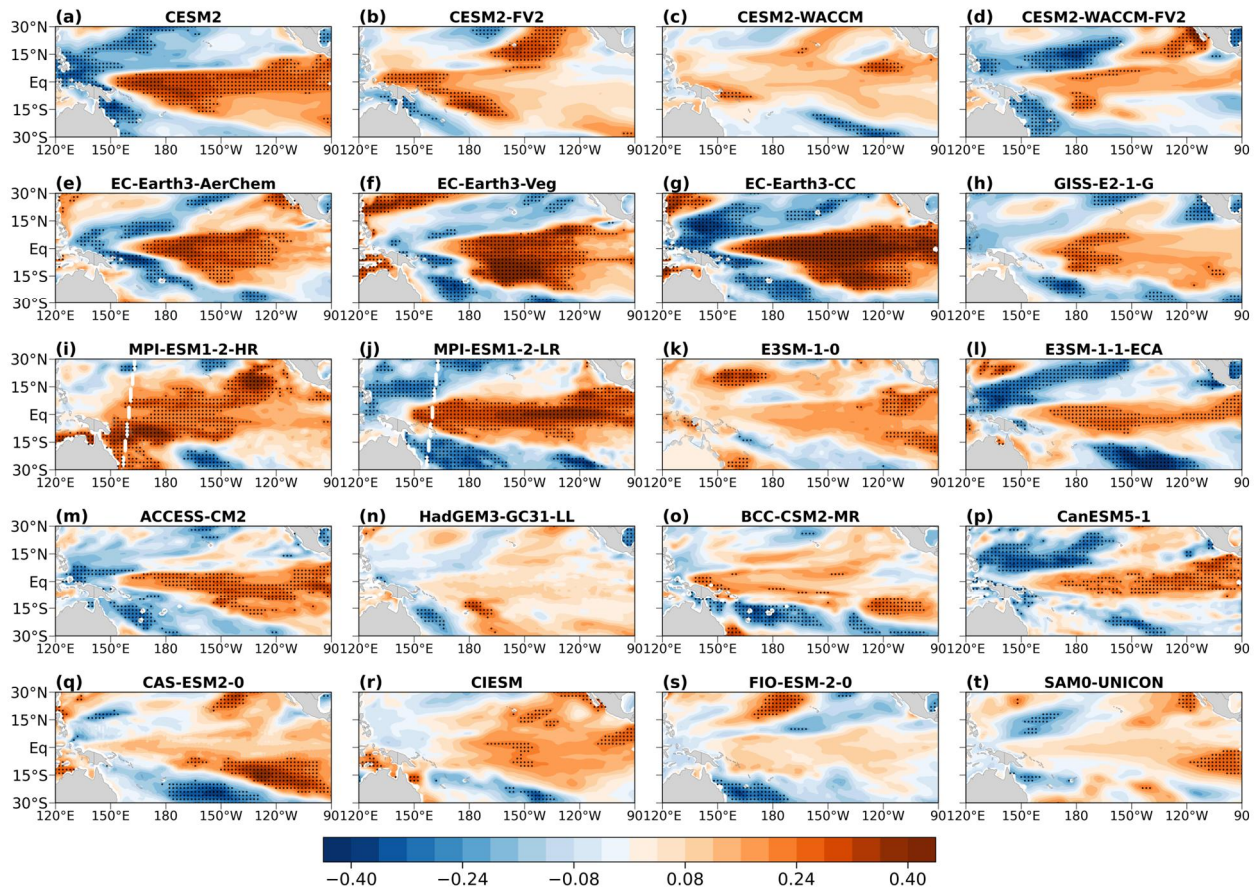
**Figure 910.** Time series of the standardized NP<sub>fit</sub> index (blue line), along with (a) July–September mean T<sub>10-30</sub> index (red line), (b) July–September mean U<sub>10-30</sub> index (red line, multiplied by -1), and (c) July–September mean TCO<sub>3</sub> index (red line) from 1981 to 2024. R in the upper right corner is the correlation coefficient between NP<sub>fit</sub> index and T<sub>10-30</sub>, U<sub>10-30</sub>, and TCO<sub>3</sub> indices, respectively.

**6 CMIP6 results**

627 To further assess the cross-seasonal effects of tropical central Pacific SST anomalies on  
628 Antarctic stratospheric temperatures, 20 CMIP6 historical fully-coupled model simulations for the  
629 period 1951-2014 are examined. Consistent with observations, the July–September mean polar-cap  
630 (60°–90°S) mean stratospheric temperature at 10 hPa ( $T_{10}$ ) exhibits a robust positive correlation  
631 with tropical central Pacific SSTs in most CMIP6 simulations (Fig.11). Statistically significant  
632 correlations are found significant in simulations from CESM2, EC-Earth3-AerChem, EC-Earth3-  
633 Veg, EC-Earth3-CC, GISS-E2-1-G, MPI-ESM-1-2-HAM, MPI-ESM1-2-LR, E3SM-1-1-ECA,  
634 ACCESS-CM2, and CanESM5-1. Although several models (e.g., CESM2-WACCM, E3SM-1-0,  
635 HadGEM3-GC31-LL, BCC-CSM2-MR, CAS-ESM2-0, FIO-ESM-2-0, SAM0-UNICON) dot not  
636 show statistically significant results, they nevertheless display a positive correlation pattern in the  
637 tropical central Pacific. In addition, the simultaneous correlations between July-September  $T_{10}$  and  
638 SSTs show a statistically significant positive correlation over the southeastern Pacific (Fig. 12).  
639 Similarly, correlations with sea-ice concentration in the Amundsen Sea and Ross Sea exhibit strong  
640 negative values in most models, although a few (e.g., EC-Earth3-AerChem, EC-Earth3-Veg,  
641 CIESM, E3SM-1-1-ECA) display weaker correlations (Fig. 13).

642 Overall, these results are consistent with observations and support the presence of a cross-  
643 seasonal linkage between tropical central Pacific SST anomalies and Antarctic stratospheric polar  
644 temperatures.

645



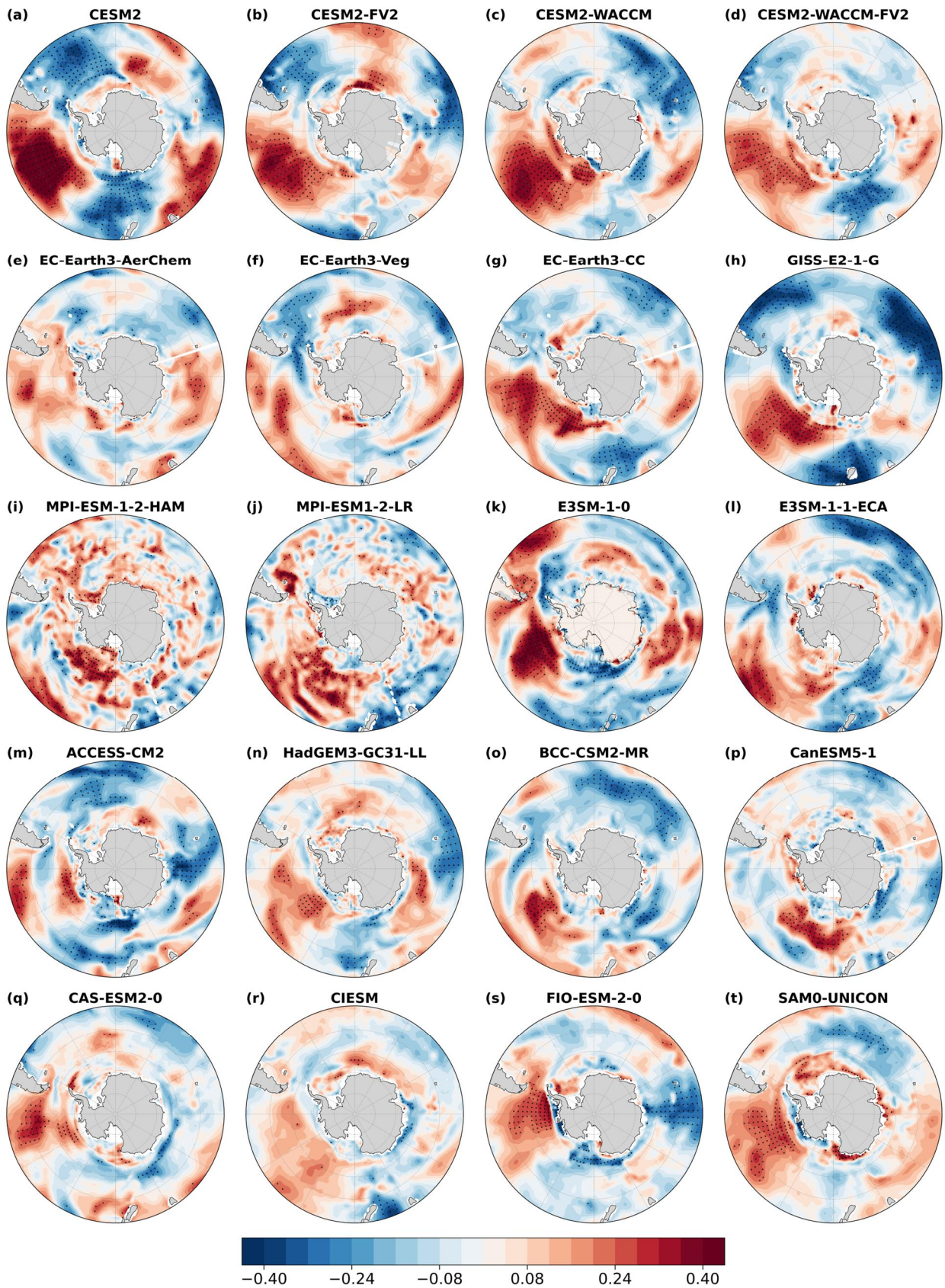
646

647

648

649

**Figure 11.** Correlation between January–March mean SST and July–September mean  $T_{10}$  index (shaded). Black dots indicate regions statistically significant at the 90% confidence level.



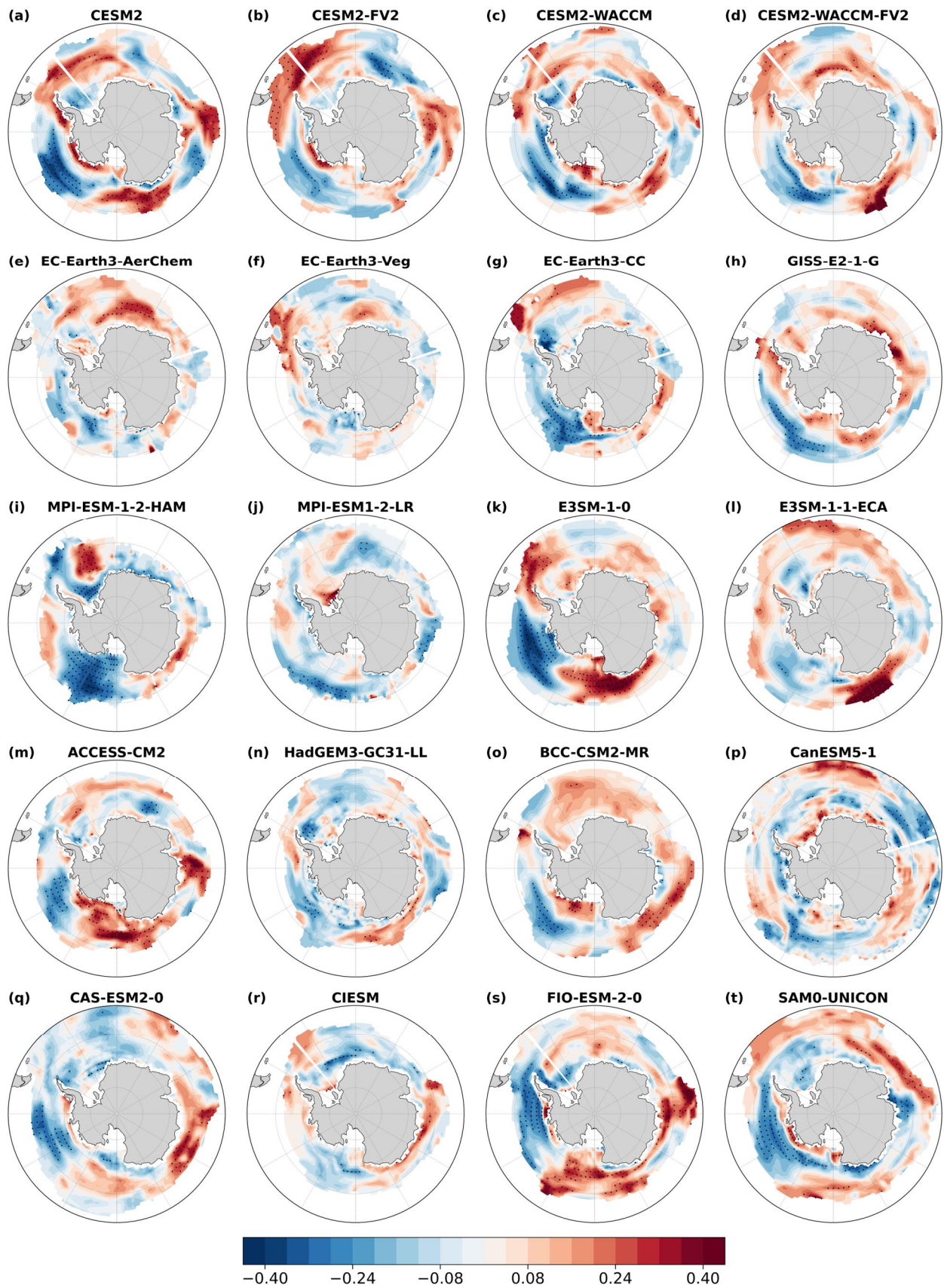
650

651

652

653

**Figure 12.** Correlation between July–September mean SST and July–September mean  $T_{10}$  index (shaded). Black dots indicate regions statistically significant at the 90% confidence level.



654

655 **Figure 13.** Correlation between July–September mean SIC and July–September mean  $T_{10}$  index (shaded). Black  
 656 dots indicate regions statistically significant at the 90% confidence level.

657

658

## 659 **6.7 Conclusions and discussions**

660 The cross-seasonal influence of the El Niño–Southern Oscillation (ENSO) on Antarctic  
 661 stratospheric circulation was investigated in this study using ERA5 reanalysis of 45 years (1980–  
 662 2024). Our analysis revealed that sea surface temperature (SST) anomalies have a significant  
 663 impact on the stratospheric temperatures. Specifically, warm (cold) SST anomalies (SSTs) in the  
 664 NiñoNiño 4 region (Central Pacific) during boreal winter are followed by significantly warming  
 665 (cooling) of the Antarctic stratosphere in the subsequent austral winter (July–September),  
 666 accompanied by a weakening (strengthening) of the stratospheric polar vortex (SPV). Among the  
 667 ENSO indices (NiñoNiño 3, NiñoNiño 3.4, NiñoNiño 4), the boreal winter NiñoNiño 4 index  
 668 exhibits the strongest and most robust correlation with the July–September polar stratospheric  
 669 temperature ( $T_{10-30}$ ) index, reaching  $R \approx 0.43$  ( $p < 0.01$ ). In contrast, correlations with NiñoNiño  
 670 3.4 and NiñoNiño 3 indices (Eastern Pacific) are substantially weaker, suggesting that NiñoNiño 4  
 671 SSTs are the primary drivers of the observed Antarctic stratospheric responses. In addition to the  
 672 observational analyses, the fully coupled simulations from 20 CMIP6 models also reproduce the  
 673 cross-seasonal connection between tropical central Pacific SST anomalies and Antarctic  
 674 stratospheric temperature anomalies, providing further evidence for the robustness of this  
 675 teleconnection.

676 The underlying dynamics involve the Pacific–South America (PSA) teleconnection pattern  
 677 triggered by NiñoNiño 4 SSTs and mediated through wave–mean flow interactions. During boreal  
 678 winter, warm SSTs in the NiñoNiño 4 region enhance convection near the dateline, exciting a  
 679 Rossby wave train that propagates poleward and eastward across the Southern Hemisphere. This  
 680 wave activity generates a positive geopotential height anomaly over the southeastern South Pacific  
 681 and a negative anomaly over the South Atlantic, reinforcing the climatological wave-1 ridge and  
 682 trough structure. As the seasonal transition into austral summer and winter progresses, the Antarctic  
 683 stratospheric circulation shifts toward a more westerly regime, creating favorable conditions for  
 684 planetary waves into the polar stratosphere. The convergence of Eliassen–Palm (E–P) fluxes,  
 685 followed by wave breaking, induces stratospheric warming and a deceleration of the SPV.

686 It was also found that warm SSTs in the South Pacific and sea-ice loss over the Amundsen and  
 687 Ross Seas can reinforce the mid and high latitudes zonal wave train through sea–air interactions.

688 Specially, PSA teleconnection associated with ~~Niño~~Niño 4 warming drives ocean heat uptake and  
 689 rising SSTs in the southeast Pacific from January-March to April-June. With progression of seasons,  
 690 this remote forcing weakens during the June-September, a local sea-air feedback becomes  
 691 dominant, persistent warm waters accelerate sea-ice melt, and the subsequent oceanic heat release  
 692 sustains the atmospheric high pressure anomaly, thereby strengthening the planetary wave anomaly.

693 Furthermore, stronger planetary wave anomalies induced by warm ~~Niño~~Niño 4 SSTs were  
 694 found to play a crucial role in modulating Antarctic ozone transport. These anomalous waves  
 695 enhance the residual circulation, facilitating the ozone transport from the tropics to the polar  
 696 stratosphere and leading to elevated ozone concentrations over Antarctica. The increased ozone  
 697 concentrations enhance ultraviolet absorption, further amplifying stratospheric warming.  
 698 Simultaneously, a warmer stratosphere inhibits the formation of polar stratospheric clouds (PSCs),  
 699 thereby suppressing the heterogeneous chemical reactions responsible for ozone depletion and  
 700 mitigating Antarctic ozone loss (Solomon et al., 2016).

701 A multivariate regression statistical model was used in this study to determine the linear  
 702 relationship between stratospheric temperature variations and ~~Niño~~Niño 4 SST. The ~~Niño~~Niño 4  
 703 index alone accounts for approximately 18 % of the variance in July–September polar stratospheric  
 704 temperatures. However, when the June PSA index, ~~June South Pacific SST (SST<sub>SP</sub>) index, and the~~  
 705 ~~May–June mean Antarctic sea-ice concentration (SIC) index~~ ~~is~~are included as additional  
 706 ~~predictor~~ factors, the explained variance nearly doubles to 35.2 %. This highlights the combined  
 707 importance of both tropical forcing and mid–latitude atmospheric responses in stratospheric  
 708 temperature ~~variability~~ predictability. ~~Such forecasts based on this multivariate regression model~~  
 709 ~~can provide lead times of up to 1–6 months for anticipating potential stratospheric warming events~~  
 710 ~~and assessing the risk of ozone depletion during the austral winter.~~

711 Nonetheless, a substantial portion of stratospheric variability remains unexplained. This  
 712 reflects the influence of atmospheric internal dynamics, as well as contributions from other drivers  
 713 such as the Quasi–Biennial Oscillation (QBO), solar activity, and mid–latitude tropospheric wave  
 714 sources. Additional ~~predictor~~ factors may be identified through a range of approaches, including  
 715 numerical modeling, machine learning, and causal inference.

716

717 **Code and data availability.**

718 The ERA5 reanalysis data are available from the European Centre for Medium-Range  
719 Weather Forecasts at Hersbach et al. (2023). ~~Niño~~Niño 4 index came from National Oceanic and  
720 Atmospheric Administration (<https://psl.noaa.gov/data/timeseries/month/DS/Nino4/>,  
721 <https://psl.noaa.gov/data/timeseries/month/DS/Nino3/>, and  
722 <https://psl.noaa.gov/data/timeseries/month/DS/Nino34/>). The code used in this article is accessible  
723 from the corresponding author.

724

### 725 **Author contributions**

726 YZ, ZL, JS, and ZX contributed to the conceptualization of the study. YZ designed the  
727 methodology, developed the software, performed the validation, formal analysis, investigation, data  
728 curation, and visualization. JS, GL, and ZX were responsible for funding acquisition, project  
729 administration, and providing the necessary resources. The work was supervised by ZL, JS, GL,  
730 WP, and ZX. YZ prepared the original manuscript with contributions from ZL, JS, WP, and ZX.  
731 All authors contributed to the review and editing of the final manuscript.

732

### 733 **Competing interests**

734 The contact author has declared that none of the authors has any competing interests.

735

### 736 **Acknowledgments**

737 The research was supported by the National Natural Science Foundation of China (42394123  
738 and 42394122), “Transforming Climate Action” program (TCA-LRP-20240B-1.1-WP6JS) led by  
739 Dalhousie University, Canada, Natural Sciences and Engineering Research Council of Canada to  
740 JS (NSERC, Grant NOs: 217081), and the China Scholarship Council (CSC, 202306340119). We  
741 also appreciate all the support provided by the Department of Oceanography, Dalhousie University.

742

### 743 **Financial support**

744 This research was supported by the National Natural Science Foundation of China (42394123  
745 and 42394122), the “Transforming Climate Action” program (TCA-LRP-20240B-1.1-WP6JS),  
746 Natural Sciences and Engineering Research Council of Canada to JS (NSERC, Grant NOs: 217081),  
747 and the China Scholarship Council (CSC, 202306340119). [Gansu Provincial Natural Science  
748 Foundation \(25JRRA323\)](#).

749

750 **References**

- 751 [Albers, J.R. and Birner, T.: Vortex Preconditioning due to Planetary and Gravity Waves prior to](#)  
 752 [Sudden Stratospheric Warmings, \*Journal of the Atmospheric Sciences\*, 71, 4028–4054,](#)  
 753 <https://doi.org/10.1175/jas-d-14-0026.1>, 2014.
- 754 Alexander, M.A., Bladé, I., Newman, M., Lanzante, J. R., Lau, N. C., and Scott, J. D.: The  
 755 Atmospheric Bridge: The Influence of ENSO Teleconnections on Air–Sea Interaction over the  
 756 Global Oceans, *Journal of Climate*, 15, 2205–2231, [https://doi.org/10.1175/1520-0442\(2002\)015<2205:tabtio>2.0.co;2](https://doi.org/10.1175/1520-0442(2002)015<2205:tabtio>2.0.co;2), 2002.
- 758 Andrews, D. G. and McIntyre, M. E.: An exact theory of nonlinear waves on a Lagrangian-mean  
 759 flow, *Journal of Fluid Mechanics*, 89, 609–646, <https://doi.org/10.1017/s0022112078002773>,  
 760 1978.
- 761 Andrews, D. G. and McIntyre, M. E.: Planetary Waves in Horizontal and Vertical Shear: The  
 762 Generalized Eliassen-Palm Relation and the Mean Zonal Acceleration, *Journal of the*  
 763 *Atmospheric Sciences*, 33, 2031–2048, [https://doi.org/10.1175/1520-0469\(1976\)033<2031:pwihav>2.0.co;2](https://doi.org/10.1175/1520-0469(1976)033<2031:pwihav>2.0.co;2), 1976.
- 765 Andrews, D. G., Holton, J. R., and Leovy, C. B.: *Middle atmosphere dynamics*, Academic Press,  
 766 115, 421–422, <https://doi.org/10.1002/qj.49711548612>, 1987.
- 767 Baldwin, M. P. and Dunkerton, T. J.: Stratospheric Harbingers of Anomalous Weather Regimes,  
 768 *Science*, 294, 581–584, <https://doi.org/10.1126/science.1063315>, 2001.
- 769 Baldwin, M. P., Ayarzagüena, B., Birner, T., Butchart, N., Butler, A. H., Charlton - Perez, Andrew J.,  
 770 Domeisen, Daniela I. V., Garfinkel, Chaim I., Garny, H., Gerber, Edwin P., Hegglin, Michaela I.,  
 771 Langematz, U., and Pedatella, Nicholas M.: Sudden Stratospheric Warmings, *Reviews of*  
 772 *Geophysics*, 59, <https://doi.org/10.1029/2020rg000708>, 2021.
- 773 Bamston, A. G., Chelliah, M., and Goldenberg, S. B.: Documentation of a highly ENSO - related  
 774 sst region in the equatorial pacific: Research note, *Atmosphere-Ocean*, 35, 367 - 383,  
 775 <https://doi.org/10.1080/07055900.1997.9649597>, 1997.
- 776 Barriopedro, D. and Calvo, N.: On the Relationship between ENSO, Stratospheric Sudden  
 777 Warmings, and Blocking, *Journal of Climate*, 27, 4704–4720, <https://doi.org/10.1175/jcli-d-13-00770.1>, 2014.
- 779 Butler, A. H. and Polvani, L. M.: El Niño, La Niña, and stratospheric sudden warmings: A  
 780 reevaluation in light of the observational record, *Geophysical Research Letters*, 38, n/a-n/a,  
 781 <https://doi.org/10.1029/2011gl048084>, 2011.
- 782 Domeisen, D. I. V., Garfinkel, C. I., and Butler, A. H.: The Teleconnection of El Niño Southern  
 783 Oscillation to the Stratosphere, *Reviews of Geophysics*, 57, 5–47,  
 784 <https://doi.org/10.1029/2018rg000596>, 2019.
- 785 Esler, J. G., Polvani, L. M., and Scott, R. K.: The Antarctic stratospheric sudden warming of 2002:  
 786 A self - tuned resonance?, *Geophysical Research Letters*, 33,  
 787 <https://doi.org/10.1029/2006gl026034>, 2006.
- 788 Evtushevsky, O. M., Kravchenko, V. O., Hood, L. L., and Milinevsky, G. P.: Teleconnection  
 789 between the central tropical Pacific and the Antarctic stratosphere: spatial patterns and time

- 790 lags, *Climate Dynamics*, 44, 1841–1855, <https://doi.org/10.1007/s00382-014-2375-2>, 2015.
- 791 Fogt, R. L., Bromwich, David H., and Hines, Keith M.: Understanding the SAM influence on the  
792 South Pacific ENSO teleconnection, *Climate Dynamics*, 36, 1555–1576,  
793 <https://doi.org/10.1007/s00382-010-0905-0>, 2011.
- 794 Garfinkel, C. I. and Hartmann, D. L.: Different ENSO teleconnections and their effects on the  
795 stratospheric polar vortex, *Journal of Geophysical Research: Atmospheres*, 113,  
796 <https://doi.org/10.1029/2008jd009920>, 2008.
- 797 Grassi, B., Redaelli, G., and Visconti, G.: Tropical SST Preconditioning of the SH Polar Vortex  
798 during Winter 2002, *Journal of Climate*, 21, 5295–5303,  
799 <https://doi.org/10.1175/2008jcli2136.1>, 2008.
- 800 Hersbach, H., Bell, B., Berrisford, P., Biavati, G., Horányi, A., Muñoz Sabater, J., Nicolas, J.,  
801 Peubey, C., Radu, R., Rozum, I., Schepers, D., Simmons, A., Soci, C., Dee, D., and Thépaut,  
802 J.-N.: ERA5 hourly data on pressure levels from 1940 to present, Copernicus Climate Change  
803 Service (C3S) Climate Data Store (CDS), Dataset, <https://doi.org/10.24381/cds.bd0915c6>,  
804 2023a.
- 805 Hersbach, H., Bell, B., Berrisford, P., Biavati, G., Horányi, A., Muñoz Sabater, J., Nicolas, J.,  
806 Peubey, C., Radu, R., Rozum, I., Schepers, D., Simmons, A., Soci, C., Dee, D., and Thépaut,  
807 J.-N.: ERA5 hourly data on single levels from 1940 to present, Copernicus Climate Change  
808 Service (C3S) Climate Data Store (CDS), Dataset, <https://doi.org/10.24381/cds.adbb2d47>,  
809 2023b.
- 810 Hu, Y. and Fu, Q.: Stratospheric warming in Southern Hemisphere high latitudes since 1979,  
811 *Atmospheric Chemistry and Physics*, 9, 4329–4340, <https://doi.org/10.5194/acp-9-4329-2009>,  
812 2010.
- 813 Hurwitz, M. M., Newman, P. A., Oman, L. D., and Molod, A. M.: Response of the Antarctic  
814 Stratosphere to Two Types of El Niño Events, *Journal of the Atmospheric Sciences*, 68, 812–  
815 822, <https://doi.org/10.1175/2011jas3606.1>, 2011a.
- 816 Hurwitz, M. M., Song, I.-S., Oman, L. D., Newman, P. A., Molod, A. M., Frith, S. M., and Nielsen,  
817 J. E.: Response of the Antarctic stratosphere to warm pool El Niño Events in the GEOS CCM,  
818 *Atmospheric Chemistry and Physics*, 11, 9659–9669, [https://doi.org/10.5194/acp-11-9659-](https://doi.org/10.5194/acp-11-9659-2011)  
819 2011, 2011b.
- 820 Ineson, S. and Scaife, A. A.: The role of the stratosphere in the European climate response to El  
821 Niño, *Nature Geoscience*, 2, 32–36, <https://doi.org/10.1038/ngeo381>, 2009.
- 822 Karpetchko, A., Kyrö, E., and Knudsen, B. M.: Arctic and Antarctic polar vortices 1957 – 2002 as  
823 seen from the ERA - 40 reanalyses, *Journal of Geophysical Research: Atmospheres*, 110,  
824 <https://doi.org/10.1029/2005jd006113>, 2005.
- 825 Kim, B.-M., Choi, H., Kim, S.-J., and Choi, W.: Amplitude-dependent relationship between the  
826 Southern Annular Mode and the El Niño Southern Oscillation in austral summer, *Asia-Pacific  
827 Journal of Atmospheric Sciences*, 53, 85–100, <https://doi.org/10.1007/s13143-017-0007-6>,  
828 2017.
- 829 Kuroda, Y., Deushi, M., and Shibata, K.: Role of solar activity in the troposphere - stratosphere

- 830 coupling in the Southern Hemisphere winter, *Geophysical Research Letters*, 34,  
831 <https://doi.org/10.1029/2007gl030983>, 2007.
- 832 L'Heureux, M. L. and Thompson, D. W. J.: Observed Relationships between the El Niño–Southern  
833 Oscillation and the Extratropical Zonal-Mean Circulation, *Journal of Climate*, 19, 276–287,  
834 <https://doi.org/10.1175/jcli3617.1>, 2006.
- 835 Laat, A. T. J., and Weele, M. V: The 2010 Antarctic ozone hole: Observed reduction in ozone  
836 destruction by minor sudden stratospheric warmings, *Scientific Reports*, 1,  
837 <https://doi.org/10.1038/srep00038>, 2011.
- 838 Lim, E. - P., Hendon, H. H., and Thompson, D. W. J.: Seasonal Evolution of Stratosphere -  
839 Troposphere Coupling in the Southern Hemisphere and Implications for the Predictability of  
840 Surface Climate, *Journal of Geophysical Research: Atmospheres*, 123, 12,002-12,016,  
841 <https://doi.org/10.1029/2018jd029321>, 2018.
- 842 Lim, E., Zhou, L., Young, G., Abhik, S., Rudeva, I., Hope, P., Wheeler, M. C., Arblaster, J. M.,  
843 Hendon, H. H., Manney, G., Son, S., Oh, J., and Garreaud, R. D.: Predictability of the 2020  
844 Strong Vortex in the Antarctic Stratosphere and the Role of Ozone, *Journal of Geophysical  
845 Research: Atmospheres*, 129, <https://doi.org/10.1029/2024jd040820>, 2024.
- 846 Lin, J. and Qian, T.: Impacts of the ENSO Lifecycle on Stratospheric Ozone and Temperature,  
847 *Geophysical Research Letters*, 46, 10646–10658, <https://doi.org/10.1029/2019gl083697>,  
848 2019.
- 849 Lin, P., Fu, Q., and Hartmann, D. L.: Impact of Tropical SST on Stratospheric Planetary Waves in  
850 the Southern Hemisphere, *Journal of Climate*, 25, 5030–5046, <https://doi.org/10.1175/jcli-d-11-00378.1>, 2012.
- 852 Lin, P., Fu, Q., Solomon, S., and Wallace, J. M.: Temperature Trend Patterns in Southern  
853 Hemisphere High Latitudes: Novel Indicators of Stratospheric Change, *Journal of Climate*,  
854 22, 6325–6341, <https://doi.org/10.1175/2009jcli2971.1>, 2009.
- 855 Ma, C., Yang, P., Tan, X., and Bao, M.: Possible Causes of the Occurrence of a Rare Antarctic  
856 Sudden Stratospheric Warming in 2019, *Atmosphere*, 13, 147,  
857 <https://doi.org/10.3390/atmos13010147>, 2022.
- 858 Manatsa, D. and Mukwada, G.: A connection from stratospheric ozone to El Niño–Southern  
859 Oscillation, *Scientific Reports*, 7, <https://doi.org/10.1038/s41598-017-05111-8>, 2017.
- 860 [Matsuno, T. A Dynamical Model of the Stratospheric Sudden Warming. \*Journal of the Atmospheric\*](#)  
861 [Sciences](#), 28(8), 1479–1494. [https://doi.org/10.1175/1520-](https://doi.org/10.1175/1520-0469(1971)028<1479:admots>2.0.co;2)  
862 [0469\(1971\)028<1479:admots>2.0.co;2](#), 1971.
- 863 McPhaden, M. J., Zebiak, S. E., and Glantz, M. H.: ENSO as an Integrating Concept in Earth  
864 Science, *Science*, 314, 1740–1745, <https://doi.org/10.1126/science.1132588>, 2006.
- 865 Mo, K.C. and Higgins, R. W.: The Pacific–South American Modes and Tropical Convection during  
866 the Southern Hemisphere Winter, *Monthly Weather Review*, 126, 1581–1596,  
867 [https://doi.org/10.1175/1520-0493\(1998\)126<1581:tpsama>2.0.co;2](https://doi.org/10.1175/1520-0493(1998)126<1581:tpsama>2.0.co;2), 1998.
- 868 Niu, Y., Xie, F., and Wu, S.: ENSO Modoki Impacts on the Interannual Variations of Spring  
869 Antarctic Stratospheric Ozone, *Journal of Climate*, 36, 5641–5658,

870 <https://doi.org/10.1175/jcli-d-22-0826.1>, 2023.

871 [O'Neill, A., and C. Youngblut.: Stratospheric warmings diagnosed using the transformed Eulerian-](#)  
 872 [mean equations and the effect of the mean state on wave propagation. Journal of the](#)  
 873 [Atmospheric Sciences, 39, 1370 - 1386, doi:10.1175/1520-0469\(1982\)039,1370:](#)  
 874 [SWDUTT.2.0.CO;2. 1982.](#)

875 Polvani, L. M., Sun, L., Butler, A. H., Richter, J. H., and Deser, C.: Distinguishing Stratospheric  
 876 Sudden Warmings from ENSO as Key Drivers of Wintertime Climate Variability over the  
 877 North Atlantic and Eurasia, *Journal of Climate*, 30, 1959–1969, [https://doi.org/10.1175/jcli-d-](https://doi.org/10.1175/jcli-d-16-0277.1)  
 878 [16-0277.1](https://doi.org/10.1175/jcli-d-16-0277.1), 2017.

879 Rao, J., Garfinkel, C. I., Ren, R., Wu, T., and Lu, Y.: Southern Hemisphere Response to the Quasi-  
 880 Biennial Oscillation in the CMIP5/6 Models, *Journal of Climate*, 36, 2603–2623,  
 881 <https://doi.org/10.1175/jcli-d-22-0675.1>, 2023.

882 Rayner, N. A., Parker, D. E., Horton, E. B., Folland, C. K., Alexander, L. V., Rowell, D. P., Kent,  
 883 E. C., and Kaplan, A.: Global analyses of sea surface temperature, sea ice, and night marine  
 884 air temperature since the late nineteenth century, *Journal of Geophysical Research:*  
 885 *Atmospheres*, 108, <https://doi.org/10.1029/2002jd002670>, 2003.

886 [Rea, D., Elsbury, D., Butler, A.H., Sun, L., Peings, Y., and Magnusdottir, G.: Interannual Influence](#)  
 887 [of Antarctic Sea Ice on Southern Hemisphere Stratosphere-Troposphere Coupling,](#)  
 888 [Geophysical Research Letters, 51, https://doi.org/10.1029/2023gl107478, 2024.](#)

889 Shen, X., Wang, L., and Osprey, S.: Tropospheric Forcing of the 2019 Antarctic Sudden  
 890 Stratospheric Warming, *Geophysical Research Letters*, 47,  
 891 <https://doi.org/10.1029/2020gl089343>, 2020.

892 Silvestri, G. and Vera, C.: Nonstationary Impacts of the Southern Annular Mode on Southern  
 893 Hemisphere Climate, *Journal of Climate*, 22, 6142–6148,  
 894 <https://doi.org/10.1175/2009jcli3036.1>, 2009.

895 Singh, A. K. and Bhargawa, A.: Atmospheric burden of ozone depleting substances (ODSs) and  
 896 forecasting ozone layer recovery, *Atmospheric Pollution Research*, 10, 802–807,  
 897 <https://doi.org/10.1016/j.apr.2018.12.008>, 2019.

898 Solomon, S., Ivy, D. J., Kinnison, D., Mills, M. J., Neely, R. R., and Schmidt, A.: Emergence of  
 899 healing in the Antarctic ozone layer, *Science*, 353, 269–274,  
 900 <https://doi.org/10.1126/science.aae0061>, 2016.

901 Song, K. and Son, S.-W.: Revisiting the ENSO–SSW Relationship, *Journal of Climate*, 31, 2133–  
 902 2143, <https://doi.org/10.1175/jcli-d-17-0078.1>, 2018.

903 [Song, J., Zhang, J., Du, S., Xu, M., and Zhao, S.: Impact of Early Winter Antarctic Sea Ice](#)  
 904 [Reduction on Antarctic Stratospheric Polar Vortex, Journal of Geophysical Research:](#)  
 905 [Atmospheres, 130, https://doi.org/10.1029/2024jd041831, 2025.](#)

906 Stone, K. A., Solomon, S., Thompson, D. W. J., Kinnison, D. E., and Fyfe, J. C.: On the Southern  
 907 Hemisphere stratospheric response to ENSO and its impacts on tropospheric circulation,  
 908 *Journal of Climate*, 35, 1963–1981, <https://doi.org/10.1175/jcli-d-21-0250.1>, 2022.

909 [Sun, L., Deser, C., and Tomas, R.A.: Mechanisms of Stratospheric and Tropospheric Circulation](#)

- 910 [Response to Projected Arctic Sea Ice Loss, Journal of Climate, 28, 7824 – 7845,](https://doi.org/10.1175/jcli-d-15-0169.1)  
911 [https://doi.org/10.1175/jcli-d-15-0169.1, 2015.](https://doi.org/10.1175/jcli-d-15-0169.1)
- 912 Takaya, K. and Nakamura, H.: A Formulation of a Phase-Independent Wave-Activity Flux for  
913 Stationary and Migratory Quasigeostrophic Eddies on a Zonally Varying Basic Flow, *Journal*  
914 *of the Atmospheric Sciences*, 58, 608–627, [https://doi.org/10.1175/1520-](https://doi.org/10.1175/1520-0469(2001)058<0608:afoapi>2.0.co;2)  
915 [0469\(2001\)058<0608:afoapi>2.0.co;2](https://doi.org/10.1175/1520-0469(2001)058<0608:afoapi>2.0.co;2), 2001.
- 916 Thompson, D. W. J. and Solomon, S.: Interpretation of Recent Southern Hemisphere Climate  
917 Change, *Science*, 296, 895–899, <https://doi.org/10.1126/science.1069270>, 2002.
- 918 Thompson, D. W. J., Baldwin, M. P., and Solomon, S.: Stratosphere–Troposphere Coupling in the  
919 Southern Hemisphere, *Journal of the Atmospheric Sciences*, 62, 708–715,  
920 <https://doi.org/10.1175/jas-3321.1>, 2005.
- 921 Thompson, D. W. J., Solomon, S., Kushner, P. J., England, M. H., Grise, K. M., and Karoly, D. J.:  
922 Signatures of the Antarctic ozone hole in Southern Hemisphere surface climate change, *Nature*  
923 *Geoscience*, 4, 741–749, <https://doi.org/10.1038/ngeo1296>, 2011.
- 924 Trenberth, K. E.: The Definition of El Niño, *Bulletin of the American Meteorological Society*, 78,  
925 2771 – 2777, [https://doi.org/10.1175/1520-0477\(1997\)078<2771:tdoen>2.0.co;2](https://doi.org/10.1175/1520-0477(1997)078<2771:tdoen>2.0.co;2), 1997.
- 926 Wang, C.: A review of ENSO theories, *National Science Review*, 5, 813–825,  
927 <https://doi.org/10.1093/nsr/nwy104>, 2018.
- 928 Wang, Z., Zhang, J., Zhao, S., and Li, D.: The joint effect of mid-latitude winds and the westerly  
929 quasi-biennial oscillation phase on the Antarctic stratospheric polar vortex and ozone,  
930 *Atmospheric Chemistry and Physics*, 25, 3465–3480, [https://doi.org/10.5194/acp-25-3465-](https://doi.org/10.5194/acp-25-3465-2025)  
931 [2025](https://doi.org/10.5194/acp-25-3465-2025), 2025.
- 932 Yang, C., Li, T., Dou, X., and Xue, X.: Signal of central Pacific El Niño in the Southern  
933 Hemispheric stratosphere during austral spring, *Journal of Geophysical Research:*  
934 *Atmospheres*, 120, <https://doi.org/10.1002/2015jd023486>, 2015.
- 935 Zhang, R., Zhou, W., Tian, W., Zhang, Y., Liu, Z., and Cheung, P. K. Y.: Changes in the Relationship  
936 between ENSO and the Winter Arctic Stratospheric Polar Vortex in Recent Decades, *Journal*  
937 *of Climate*, 35, 5399–5414, <https://doi.org/10.1175/jcli-d-21-0924.1>, 2022.
- 938 Zi, Y., Long, Z., Sheng, J., Lu, G., Perrie, W., and Xiao, Z.: The Sudden Stratospheric Warming  
939 Events in the Antarctic in 2024, *Geophysical Research Letters*, 52,  
940 <https://doi.org/10.1029/2025gl115257>, 2025.
- 941 Zubiaurre, I. and Calvo, N.: The El Niño–Southern Oscillation (ENSO) Modoki signal in the  
942 stratosphere, *Journal of Geophysical Research: Atmospheres*, 117,  
943 <https://doi.org/10.1029/2011jd016690>, 2012.

944